

CHALMERS



Load Evaluation at Assembly of a Subsea Tie-in System

Master's Thesis in *Applied Mechanics*

MATTIAS HAGGÄRDE

Department of Applied Mechanics

Division of Dynamics

CHALMERS UNIVERSITY OF TECHNOLOGY

Gothenburg, Sweden 2013

Master's Thesis 2013:82

MASTER'S THESIS IN APPLIED MECHANICS

Load Evaluation at Assembly of a
Subsea Tie-in System

MATTIAS HAGGÄRDE

Department of Applied Mechanics

Division of Dynamics

CHALMERS UNIVERSITY OF TECHNOLOGY

Gothenburg, Sweden 2013

**Load Evaluation at Assembly of a
Subsea Tie-in System**

MATTIAS HAGGÄRDE

©MATTIAS HAGGÄRDE, 2013

ISSN 1652-8557

Master's Thesis 2013:82

Department of Applied Mechanics

Division of Dynamics

Chalmers University of Technology

SE-412 96 Gothenburg

Sweden

Telephone: +46 (0)31 - 772 1000

Cover:

The horizontal connection system for rigid jumper spools
developed by Aker Solutions during hoisting.

Gothenburg, Sweden 2013

*There's nothing wrong with enjoying looking at the surface of the ocean itself,
except that when you finally see what goes on underwater,
you realize that you've been missing the whole point of the ocean.
Staying on the surface all the time
is like going to the circus and staring at the outside of the tent.*

– Dave Barry

Abstract

Subsea technology can briefly be described as the technology for exploration, drilling and development of oil and gas in underwater locations. Structures commonly located at the surface are placed at the seabed and connected with a tie-in system which allows flow of water and hydrocarbons as well as hydraulic and electric communication between them. In this thesis, the assembling of a system for connecting a horizontally positioned jumper spool¹ to a subsea structure is considered.

During assembling, several loads act on the system. In order to increase the understanding of the system's behaviour and the loads acting on its parts, simulations are performed on a simplified FE-model in Abaqus[®], constituted of connector elements and solid representation of the interacting parts. Loads and positions are measured at various locations on the model throughout the simulation. A method is developed for evaluating whether or not the assembling shall be accepted, given the measures and a defined acceptance criterion.

Furthermore, the possibility of using substructures² in a simplified model of the system is investigated through implementation of two additional FE-models; one utilising solid parts only and one utilising a combination of substructures and solid parts. The analysis shows that the FE-model implemented with substructures performs equally well as the FE-model implemented with only solid parts and that it is approximately 33 % less CPU intensive. However, Abaqus[®] does not allow thread-based parallel processing of all operations if substructures are present, why it is almost three times as resource intensive overall. The FE-model utilising connector elements is approximately 20 % less resource intensive than the FE-model constituted of only solid elements but is subject to more noise and gives results which differ up to 10 % as compared with the FE-model constituted of solid parts only.

It is concluded that some parts can be modelled with substructures without significantly affecting the result, but do only decrease the overall computation cost if parallel processing is possible. Using connector elements to simplify the model introduces more noise and additional uncertainties in the model. The result differs significantly as compared with the FE-model constituted of only solid parts and the decrease in computation cost is not very large.

Keywords: Subsea, Offshore, Tie-in, FEM, Finite Element, Superelement, Substructure

¹A jumper spool is a rigid flowline for water or hydrocarbons.

²Also known as superelements.

Contents

1	Introduction	1
1.1	Background	1
1.2	Purpose	2
1.3	Limitations	3
1.4	Thesis Outline	3
2	Connection System	4
2.1	Horizontal Connection System – HCS-R	4
2.2	Stroking Acceptance Criterion	6
3	Conceptual Framework	8
3.1	System of Equations	8
3.2	Elements	9
3.2.1	Hourglassing	10
3.3	Connector Elements	11
3.4	Constraints	12
3.5	Contact Interactions	12
3.6	Substructures	14
3.7	Material Model	15
3.8	Solver Procedure	16
4	FE-model Implementation	18
4.1	Connector Elements Model	18
4.1.1	Connections, Constraints and Contacts	20
4.1.2	Boundary Conditions	21
4.1.3	Springs and Dampers	21
4.1.4	Loads	22
4.1.5	Steps	24
4.1.6	Base Load Case	24
4.2	Substructures Model	25
4.3	Solid Parts Model	27
4.4	Elements for Solid Parts	27
4.5	Definitions	27
4.6	Pre-simulations	29
4.6.1	Static vs. Dynamic Simulation	29
4.6.2	Time Frame	30

4.6.3	Material Implementation	32
4.6.4	Stabilising the Model	32
4.6.5	Integration Order	32
4.6.6	Controlled Displacement vs. Controlled Force	33
4.7	Mesh Convergence	33
4.7.1	Concluding Remarks for Mesh Convergence	38
5	Results	39
5.1	System Behaviour	39
5.1.1	Results Interpretation	39
5.1.2	Altering Jumper Stiffness	43
5.1.3	Evaluation of Acceptance Criterion	46
5.1.4	Altering Friction Coefficients	47
5.1.5	Back-tension Modelling	49
5.2	Model Evaluation	53
5.2.1	Results Comparison	53
5.2.2	Computation Cost	54
6	Discussion	56
6.1	System Behaviour	56
6.1.1	Interpretation	56
6.1.2	Sensitivity	57
6.1.3	Jumper Modelling	57
6.1.4	Evaluation of Capacity	58
6.2	Model Evaluation	60
6.2.1	Results Comparison	60
6.2.2	Computation Cost	60
7	Concluding Remarks	62

List of Figures

1.1	Subsea field & HCS-R system.	2
2.1	The HCS-R system.	5
2.2	Installation and assembling of the HCS-R system.	5
2.3	Clamp connector catch measures.	6
3.1	Hourglassing & Connector element.	10
3.2	Contact characteristics.	13
3.3	CSubstructuring.	15

3.4	Material model & Solver procedure.	16
4.1	Plastic strain curves.	19
4.2	Connector elements model.	20
4.3	Connector element–constraint connection & Contact interactions.	22
4.4	Loads acting on the termination.	23
4.5	Substructures model, Porch & Termination.	26
4.6	Definitions of relative positions and reaction loads	28
4.7	Critical rod-to-funnel contact.	30
4.8	F^{Stroke} , pre-study.	31
4.9	F_x^{Reac} in funnel, pre-study.	31
4.10	α_y , pre-study.	32
4.11	Meshes for mesh convergence study.	34
4.12	Reaction force, F_x^{Reac} , mesh convergence study.	35
4.13	Reaction moment, M_y^{Reac} , mesh convergence study.	36
4.14	Mesh convergence simulation.	37
4.15	von Mises stresses for different meshes.	37
5.1	d_x^{Rel} , base load case.	40
5.2	d_z^{Rel} , base load case.	40
5.3	α_y , base load case.	41
5.4	F^{Stroke} and F_x^{Reac} , base load case.	41
5.5	F_z^{Reac} , base load case.	42
5.6	M_y^{Reac} , base load case.	42
5.7	M_y^{Jump} , base load case.	43
5.8	$d_{x,y}^{\text{Rel}}$ for hubs the last 50 mm of stroking.	44
5.9	M_y^{Jump} for $\alpha_y = \alpha_{y,s}^\circ$ initially.	44
5.10	M_y^{Jump} for $\alpha_y = -\alpha_{y,s}^\circ$ initially.	45
5.11	α_y for $\alpha_y = \alpha_{y,s}^\circ$ initially.	45
5.12	α_y for $\alpha_y = -\alpha_{y,s}^\circ$ initially	45
5.13	F^{Stroke} for $\alpha_y = \alpha_{y,s}^\circ$ initially.	46
5.14	F^{Stroke} for $\alpha_y = -\alpha_{y,s}^\circ$ initially.	46
5.15	F^{Stroke} for different friction coefficients settings.	48
5.16	M_y^{Jump} for different friction coefficients settings.	48
5.17	Sensitivity w.r.t. friction coefficients.	49
5.18	F^{Stroke} for various modelling of back-tension.	50
5.19	F_x^{Reac} in funnel for various modelling of back-tension.	50
5.20	Simulated stroking procedure.	52
5.21	F^{Stroke} for various modelling of reaction plates.	53
5.22	M_y^{Jump} for various modelling of reaction plates.	54
5.23	d_z^{Rel} of hubs for various modelling of reaction plates.	54
6.1	Correction factor.	58

List of Tables

4.1	Material properties.	19
4.2	Plastic strain tabular data.	19
4.3	Models for pre-analysis.	29
4.4	Mesh data for pre-analysis.	35
5.1	Sensitivity w.r.t. friction coefficients.	49
5.2	Computation cost.	55

Preface

This report was written at Aker Solutions AB (AKS) in Gothenburg during the fall of 2013. The subject was suggested by AKS in order to coincide with physical tests, initially planned to start during the autumn. Unfortunately, the tests were delayed and could therefore not be included in this report.

Due to protection of intellectual property, the true values for the acceptance criterion are replaced with fictive values. The fictive values are used throughout the report for illustrative purposes. Also, the capacity of the system is evaluated through a relation between the force generated by the tool used to assemble the system (stroking force) and the maximum allowed bending moment acting on the system (jumper moment). This relation is intellectual property and, therefore, values are only shown for the stroking force. The values for tilt angle, catch angle, and the calculated values of the jumper moment are replaced with symbolic expressions where applicable.

Several people have contributed with valuable inputs, help and support for this thesis. I would like to express the deepest appreciation to my examiner at Chalmers, Associate Professor Peter Folkow. In addition, I would like to thank Joakim Asklund at Simulia for support and guidance with Abaqus[®]. Furthermore, my grateful thanks goes to the people at AKS, in particular Markus Wallentin and Nils Ipsen, for support and valuable discussions. Finally, I would like to express my very great appreciation to Per Kron and Per Bodforss at AKS for believing in me and giving me the opportunity to accomplish this thesis.

Mattias Haggärde
Gothenburg, St. Lucia's Day, 2013

Abbreviations

Abbreviation	Description		
AKS	Aker Solutions AB		
DOF	Degree of freedom		
HCS-R	Horizontal Connection System for rigid jumper spools		
Symbol	Description	SI-unit	Report unit
α_y	Termination tilt angle	rad	deg
β_{catch}	Clamp connector catch angle	rad	deg
C	Damping matrix	Ns/m	kNs/mm
c	Linear damping coefficient, axial damper	Ns/m	kNs/mm
d^{Rel}	Relative position	m	mm
E	Energy	J	kJ
ϵ	Strain	1	1
F^{BT}	Jumper back-tension	N	kN
F^{Reac}	Reaction force	N	kN
F^{Stroke}	Stroking force	N	kN
K, k	Stiffness matrix*	N/m	kN/mm
k	Linear elasticity coefficient, axial spring	N/m	kN/mm
κ	Linear elasticity coefficient, torsion spring	Nm/rad	kNm/deg
L	Linear transformation matrix	-	-
M	Mass matrix	kg	metric tonne
M^{Jump}	Moment on termination from jumper	Nm	kNm
M^{Reac}	Reaction moment	Nm	kNm
μ	Friction coefficient	1	1
N	Number of DOFs	-	-
n_g	Number of integration points	-	-
P	External load vector	N	kN
s	Stroking length	m	mm
s_h	Distance between hubs' centres	m	mm
σ	Stress	Pa	MPa
U, u	Node displacements*	m	mm

* Structural level and element level respectively

Nomenclature

Term	Explanation
Hexahedron elements	Solid rectangular elements, “brick” elements
Jumper spool	Rigid flowline that connects subsea structures
Model	The entire finite element model, incl. settings for solution procedure, load case, initial position etc.
Part	One part of the structure, interacts with other parts
Porch	The side of the connection system that is attached the subsea structure, contains: porch reaction plate, rods and inboard hub
Stroking tool	Hydraulic tool for assembling termination and porch
Structure	The entire mechanical system that is modelled
Terminations	The side of the connection that is attached to the jumper spool, contains: termination reaction plate, funnels, termination supports and outboard hub
Tetrahedron elements	Solid elements with the shape of three sided pyramids

Section 1

Introduction

In this section, a brief background to the problem is given and the studied object is presented. Thenceforth, problem for the thesis is presented and a purpose is formulated. An outline of the thesis concludes the section.

1.1 Background

As existing oil and gas reservoirs are depleted, the global demand for oil, gas and hydrocarbon based products increases, which in turn enhance the required hydrocarbon extraction rate. Increasing recovery rate¹ and extracting oil and gas from more remote and inaccessible locations are possible solutions, but they also imply new technological challenges. Subsea technology gives access to offshore oil reservoirs located where the surface conditions are harsh or the sea depth is large.

Subsea technology can briefly be described as the technology for exploration, drilling and development of oil and gas in underwater locations. That is, equipment commonly located on the surface are instead placed at the seabed, as illustrated in Figure 1.1a, from where they operate.

When a subsea field is constructed, christmas trees² and subsea structures are located on the seabed and connected with a tie-in system. Such a system consists of flowlines for hydrocarbon and water, which are connected to the christmas trees and subsea structures with a connection system. The flowlines can be rigid or flexible with different length and shape depending on circumstances and requirements. A short rigid flowline is called *jumper spool*, or simply *jumper*.

In this thesis a Horizontal Connection System for rigid jumper spools (HCS-R) developed by Aker Solutions (AKS) is considered. A rendered illustrations of the system is shown in Figure 1.1b. The reader is referred to Section 2, *Connection System* for a more detailed description of the system and to Figures 2.1 and 2.2 for further illustrations of it.

Basically, the system consists of two parts; a termination to which the jumper is attached, and a porch attached to the subsea structure or the christmas tree. To assemble the system, the termination and porch are stroked together (assembled)

¹The recovery rate is the proportion of hydrocarbons that can be extracted from the reservoir given in percent. Commonly the recovery rate for crude oil varies between 10 % and 50 % depending on location and methods used [15].

²A christmas tree is an assembly of valves, spools and fittings placed on top of a well. Its purpose is to control the flow.

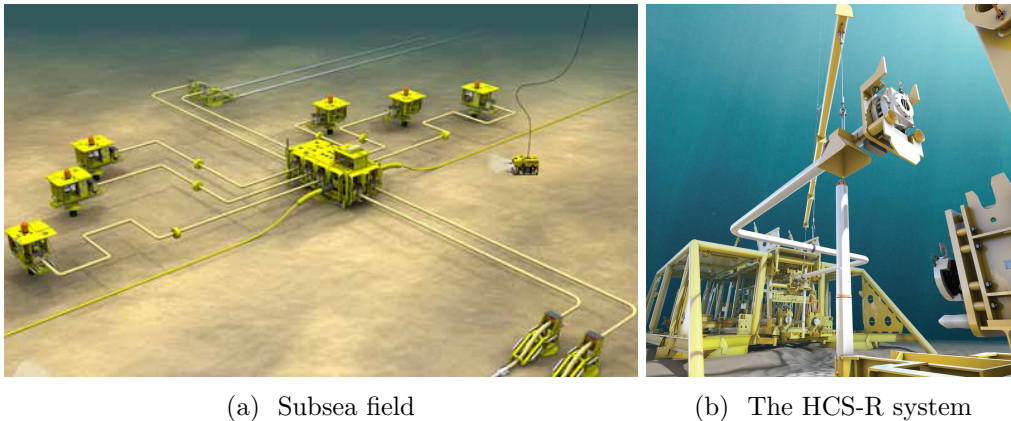


Figure 1.1: Illustration of a subsea field to the left. To the right the horizontal connection system (HCS-R) during hoisting of the jumper with the attached termination, the porch is visible to the very right.

with a special tool whereafter the system is clamped with a clamp ring to create a sealed connection.

1.2 Purpose

Simulations and FE-analyses can be carried out to ensure a well operating stroking mechanism and sufficient strength of the HCS-R system. Characteristics of the jumper and the subsea structures imply that a number of parameters affect the possibility to obtain a tight connection. Parameters such as: displacements, angle deviations, bending moments and axial and shear forces in the jumper, have to be considered when defining the load cases to be studied in the FE-analyses. Hence, there are many load cases to be studied and the analyses become rather time consuming.

In order to reduce the computation cost for the analyses, AKS has suggested that a simplified FE-model of the termination, porch, landing frame and jumper should be created by combining super elements³ and connector elements⁴ with common solid parts and contacts. The most critical load cases can later on be studied in more detail, either in a local study of the critical part or in a full study for the specific load case. This thesis aims to implement a simplified FE-model and further analyse the loads on the HCS-R system described above through simulations of the stroking procedure in Abaqus[®].

The purpose of the thesis can be summarised as:

- Investigate how a simplified FE-model of the HCS-R system, comprised of solid parts, connector elements and super elements, can be used to analyse the stroking procedure.

³See Section 3.6, *Substructures*.

⁴See Section 3.3, *Connector Elements*.

- Develop a methodology for how to implement super elements and connector elements in the FE-model using Abaqus[®].
- Obtain load curves at contact regions between porch and termination in order to improve the understanding of the load distribution on the system during stroking and to be used in future analysis of the critical load cases.

1.3 Limitations

This thesis is limited to consider a symmetric model of the HCS-R system, implemented utilising symmetry boundary conditions, see Section 4, *FE-model Implementation*.

1.4 Thesis Outline

1, Introduction

The background of the problem and the purpose of the thesis are presented.

2, Connection System

A description of the considered mechanical system, HCS-R, is given. The acceptance criterion for the stroking procedure used in this thesis is defined.

3, Conceptual Framework

Introduction to different features and modelling techniques used for the FE-model.

4, FE-model Implementation

A thorough description of how the FE-model is implemented. Results from pre-simulation are presented and various technical aspects, simplifications and potential modelling problems are discussed.

5, Results

The simulation results in terms of load curves and model sensitivity are presented and interpreted. Three different models are compared in terms of accuracy and computation cost.

6, Discussion

The results are discussed further and suggestions for improvements of the models are given.

7, Concluding Remarks

The conclusions of the thesis are given.

Section 2

Connection System

This section presents the considered mechanical system; the Horizontal Connection System for 12” rigid jumper spools – HCS-R. The parts of the system and the denotions are presented, followed by a step-by-step description of the connection procedure. In the last section, an acceptance criterion for the stroking is presented.

2.1 Horizontal Connection System – HCS-R

When a subsea field is constructed, various subsea structures are first placed at the seabed. The structures are then connected to each other with a tie-in system, comprised of *flowlines*, *jumper spools* and *umbilicals*. Flowlines and jumper spools are used for flow of water and hydrocarbons while umbilicals are used for hydraulic and electric communication between the structures. Remote operation of the equipment and tools used for installation makes it possible to operate at very large depth; up to several thousand metres. Commonly, remotely operated underwater vehicles are used to operate the tools during the installation.

Local circumstances determines the requirements on design and functionality of the tie-in system. Hence, systems with various properties are available for connecting the flowlines, jumpers or umbilicals to the structures. AKS has developed a system for connecting a rigid jumper spools horizontally to a subsea structure; the HCS-R system. This system is illustrated in Figure 2.1.

Connecting a jumper to a subsea structure with the HCS-R system can be described by the three steps below. The focus of the thesis is on the stroking in the second step.

1. The jumper is lowered from the surface using a spreader beam hanged in wires. A guide funnel on the termination (jumper side) is aligned with a guide post on the porch (structure side). The jumper is lowered further until the termination lands on the landing frame. This aligns the termination and the porch. In Figure 2.2a, the HCS-R system is shown in the position at the end of this stage. Note that the spreader beam is not included in the figure.
2. The spreader beam is released and a stroking tool is placed in position between the slots. A remotely operated underwater vehicle is used to operate the stroking tool and stroke the termination towards the porch until the inboard and outboard hubs are connected. The alignment rods and funnels guide the termination during the stroke. In Figure 2.2b the HCS-R system is shown with the stroking tool in position.

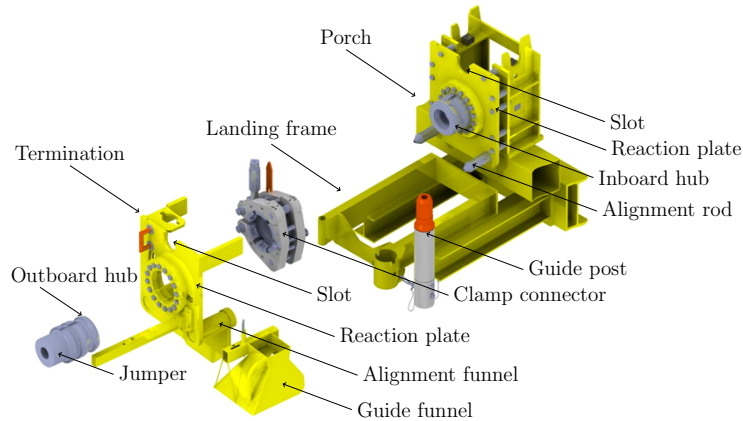


Figure 2.1: Detailed illustration of the horizontal connection system (HCS-R). The stroking tool (not illustrated) is placed between the two slots.

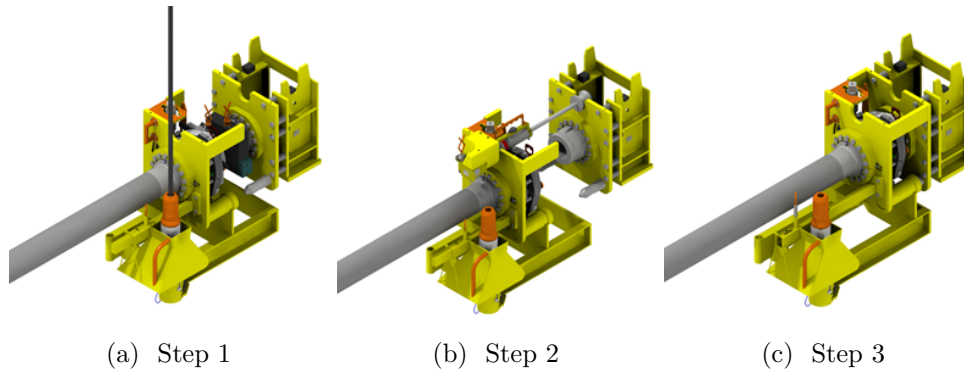


Figure 2.2: Installation and assembling of the HCS-R system.

3. A torque tool is used to close a clamp ring around the inboard and outboard hubs to seal the connection. The assembled HCS-R system is depicted in Figure 2.2c.

At the stage before stroking, no significant stresses and deformations are expected in the jumper. Stresses and deformations are, however, introduced in the jumper while stroking the termination towards the porch. To allow for such deformation, the jumper spool is usually designed with several 90° bends, as can be seen in Figures 1.1a and 1.1b, which also allows thermal expansion in the jumper spool.

Deviations from the structures' intended positions, production tolerances and the own weight of the jumper can introduce adverse forces and moments that may misalign the termination. The capacity of the stroking tool for the 12" HCS-R system is limited to 45 ton, or 440 kN. If the misalignment or the adverse forces and moments become too large, the capacity of the stroking tool may be exceeded and the system will not connect properly. Further, misalignments and adverse forces and moments may cause other problems such as: parts of the HCS-R system break due to large stresses, the connection does not seal properly or the packer located

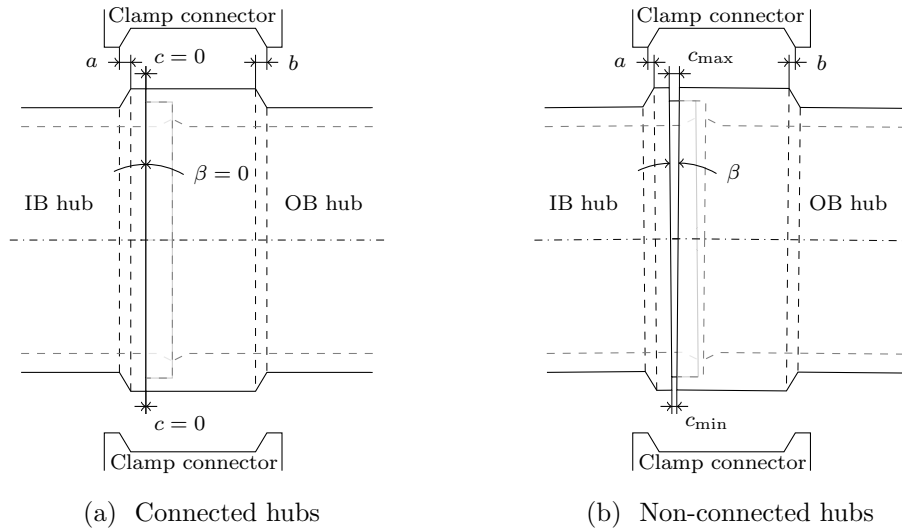


Figure 2.3: Illustration of the measures used to define clamp connector catch. Perfectly connected hubs in (a) implies $c = 0$ and $\beta = 0$.

between the inboard and outboard hubs is damaged.

2.2 Stroking Acceptance Criterion

The force generated by the stroking tool pulls the termination towards the porch, or the outboard hub towards the inboard hub. Thereafter, another mechanical feature, the *clamp connector*, is used to finalise the assembly of the connection system and ensure that the connection is sealed. The clamp connector seizes around the two hubs and pushes them together to generate a tight connection. A packer or seal located between the hubs helps to seal¹. For the clamp connector to be able to grab the hubs and create the connection, the outboard hub has to be within a certain range from the inboard hub. This range is defined as the *clamp connector catch*, or simply *catch*.

To simplify it, clamp connector catch says that the hubs have to be sufficiently close and aligned. Figure 2.3 illustrates a set of measures that can be used to define the catch. Note that the hubs themselves are axisymmetric (except for keyways that do not affect the argumentation) but since the hubs may be misaligned, the entire structure is not.

The clearance between the hubs and the clamp connector is given by $a + b$. The maximum value of the clearance is thus given by the constant $e = \max(a + b)$, achieved when the hubs are in perfect contact, as illustrated in Figure 2.3a. This implies that the maximum allowable value for c cannot exceed the constant e at any point along the circumference of the hubs for the clamp connector to be able to seize the hubs. For simplicity, in this thesis the hubs are assumed to be within catch

¹The hub seal has been left out from the analysis.

if² $c_{\max} \leq 10$ mm. The maximum diameter of the outboard hub is approximately 400 mm. Further, the hubs must be aligned for the the inboard hub to be fitted within the outboard hub's lip in order to ensure that the hubs will connect properly. For $\max(c) \leq 10$ mm this is automatically achieved since the width of the outboard hub's lip is wider than 10 mm.

Also, an acceptance criterion must be set to the misalignment angle, β . In this thesis, the fictive value of $\beta \leq \beta_{\text{catch}}^\circ$ is used.

²This is a fictive value used for illustrative purposes in this thesis only.

Section 3

Conceptual Framework

This section starts with a short introduction to the system of equations for a general dynamic FE-problem. Next the concepts of the modelling tools and techniques are presented; elements, constraints, contact interactions, connector elements and substructures. The section is finalised with descriptions of the material model and the solution procedure used in Abaqus[®].

For more extensive theory about the features presented here, the reader is referred to for example Cook et. al. [5] or Ottosen and Petterson [7]. Specific theory and guidelines for the implementation in Abaqus[®] is well presented in the Abaqus manuals [8, 9, 10, 11, 12, 13, 14].

3.1 System of Equations

The basic equation for a general dynamic finite element problem with N degrees of freedom, written on matrix form, is given by

$$\mathbf{M}\ddot{\mathbf{U}} + \mathbf{C}\dot{\mathbf{U}} + \mathbf{K}\mathbf{U} = \mathbf{P}, \quad (3.1)$$

where \mathbf{M} is the mass matrix, \mathbf{C} is the damping matrix and \mathbf{K} is the stiffness matrix, all in $\mathbb{R}^{N \times N}$ [5]. $\mathbf{P} \in \mathbb{R}^N$ is the external load vector and is, in general, time dependent. $\mathbf{U} \in \mathbb{R}^N$ contains the nodal displacements in the direction of the degrees of freedom (DOFs). Hence, the first time derivative, $\dot{\mathbf{U}}$, is the velocity and the second time derivative, $\ddot{\mathbf{U}}$, is the acceleration.

If the \mathbf{M} , \mathbf{C} and \mathbf{K} only contain constants, the system is a set of second order linear ordinary differential equation with constant coefficients. \mathbf{M} , \mathbf{C} and \mathbf{K} calculated based on the shape of the initial geometry which implies that the deformations are considered to be perturbations around the initial state, for which the matrices are calculated. If the deformations cannot be considered small, the linear perturbation assumption is no longer valid. For such problems the matrices become dependent on the displacements, \mathbf{U} , and the system becomes is a set of second order non-linear ordinary differential equations. Further, the stiffness and damping matrices depends on material properties which are deformation independent only in an idealised case where a linear stress–strain relation is assumed. Consequently, if more advanced material models are used the response will be non-linear. Examples of typical non-linear material effects are plasticity and non-linear elastic stress–strain relation. If the contacts between parts are present in the structure, its response is non-linear also for small deformations. Contacts can further imply that the matrices become unsymmetric [13].

To solve a non-linear system of equations of the form of equation (3.1) with \mathbf{M} , \mathbf{C} and \mathbf{K} dependent on \mathbf{U} , a common approach is to use an iterative solver method, for example Newton’s method¹ or any of the variations of Newton’s method [5].

3.2 Elements

There are numerous types of elements available for mechanical finite element analysis, suitable for different types of analyses. Variations in shape and number of DOFs allow for efficient modelling of various geometries. Numerical aspects such as the integration scheme and the base function’s order affect the accuracy of the model as well as computation cost.

It is common to use structural elements such as trusses, beams and shells, where applicable [7]. These elements are simplifications of the actual three dimensional geometry and can be used where simplifying assumptions about the geometry can be made. In order to model a more general body, solid elements that extend in three dimension have to be used. The most common elements are tetrahedron elements and hexahedron elements (also known as “brick” elements) [5].

Tetrahedron elements are general in the sense that any possible three dimensional shape can be meshed with them. Unfortunately there is no guarantee that the mesh becomes well structured. Also, it can be difficult to locate the element such that the element boundaries coincide with load directions. If the shape of the model is sufficiently regular, it can be meshed with hexahedron elements. Hexahedron elements require, in general, a little more work to implement but can, when implemented properly, give a nice structured mesh. The linear eight nodes hexahedron element is the simplest brick type element [14]. Each node has three DOFs, translation in x -, y - and z -direction. Since the eight node hexahedron element has only translation DOFs, bending of a structure is modelled by consecutive translations of neighbouring elements [5].

To compute the element stiffness matrix, $\mathbf{k} \in \mathbb{R}^{n \times n}$ (with $n = 24$ for an eight node hexahedron element), a numerical integration is performed over the volume of the element. The value of the integration is usually calculated by Gauss quadrature; the integral of a function f over a set Ω is approximated by

$$\int_{\Omega} f(x) = \sum_{k=1}^{n_g} w_k f(x_k), \quad (3.2)$$

where $x_k \in \Omega$, $k = 1, \dots, n_g$ are discrete integration points and w_k are weight factors [7]. It can be shown that a set $\{x_k, w_k\}$ exists, such that the approximation is the best possible given the number of integration points. Further, if f is polynomial, the integral is calculated exact if the degree of f is $2n_g - 1$ or less. In Abaqus[®] one or eight integration points can be used for the eight node linear hexahedron element, corresponding to first and second order integration respectively [12].

¹Also known as Newton-Raphson method.

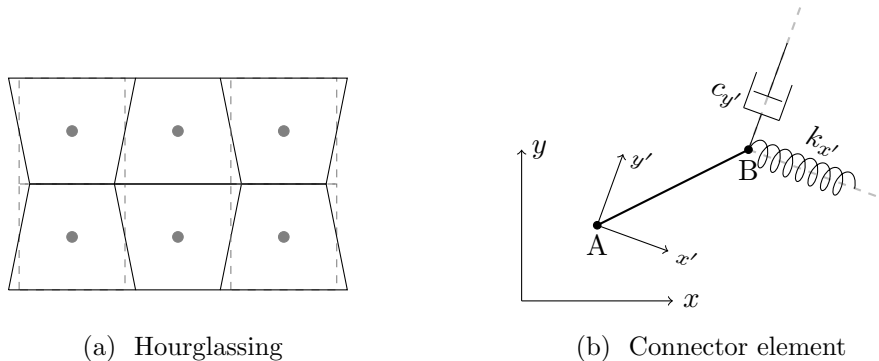


Figure 3.1: Hourglassing of a set of two dimensional four node bilateral elements in (a), based on a figure in [5]. Schematic illustration of a cartesian connector element with linear elasticity $k_{x'}$ in x' -direction and linear damping $c_{y'}$ in y' -direction in (b).

3.2.1 Hourglassing

It is desirable to have few integration points in order to reduce computation cost [12]. However, fewer integration points reduce the accuracy of the solution and the number of points is chosen as a compromise between accuracy and computation cost. Furthermore, using few integration points can lead to instabilities, also known as hourglass modes or a zero-energy modes. That is, there exist an element displacement vector \mathbf{u} , which is not a rigid body mode, such that the internal energy for the element $U_{\text{int}} = \mathbf{u}^T \mathbf{k} \mathbf{u} = 0$, where \mathbf{k} is the element stiffness matrix [5]. The existence of such a displacement vector is of course not physically correct but is a pure mathematical implication of the finite element formulation and the numerical integration scheme.

Figure 3.1a illustrates hourglassing for a set of neighbouring bilinear elements, that is rectangular plane elements with each shape function a product of two linear polynomials. The total internal energy for the six elements in the figure is zero although strains are present.

Using a Gauss-quadrature of order two or higher, in bilinear plane elements $n_g \geq 4$, eliminates the problem. The discussion above applies also for linear hexahedron elements (quadrilateral elements), where the shape functions are products of four linear polynomials. To avoid the risk of hourglassing, second order Gauss quadrature, that is at least eight integration points, $n_g = 8$, shall be used [5].

It is worth to note that since displacement based finite element formulations restrict the response of the element to a limited number of DOFs, the element stiffness is always overestimated. This sort of stiffening behaviour is also known as shear locking and volumetric locking. Reducing the number of integration points also reduce the stiffness of the element. Thus the modelled stiffness can in some cases be closer to the real value when reduced integration is used [5].

3.3 Connector Elements

A connector element is a one dimensional element that is used to connect two nodes in space utilising some attributes [13]. The first node is considered the reference point and the displacement, velocity and acceleration of the second node depends on the first node and the attributes assigned to the connector element's DOFs. The nodes can be defined in the model's global coordinate system or in local coordinate systems, separate for each node. This allows easier implementation of the properties of the connector element if it is not aligned with the global coordinate system. As an optional implementation, a connector element can be defined as one single node connected to "ground".

The type of the connector element defines which translations and rotations can be assigned attributes. It also defines possible restrictions on the DOFs. Types available are for example [13]:

- *Axial* – Attributes can be assigned to the translation DOF in the direction of the line between the two nodes.
- *Cartesian* – Attributes can be assigned to all three translation DOFs.
- *Rotation* – Attributes can be assigned to rotation DOFs in all three directions.
- *Planar* – The motion of the second node is restricted to translations in- and rotations around an axis normal to a plane defined by the first node and its assigned coordinate system. Attributes can be assigned to the allowed translations and rotation DOFs.

Of course there are many more types available. Types can be combined to generate new connector types. A typical example is the *beam* connector element which is a combination of the cartesian and rotation type. Attributes can thus be assigned to all six DOFs.

The attributes are for example physical properties such as elasticity, stiffness and damping. A connector element can be defined as rigid which implies that the stiffness is infinitely large. If attributes can be assigned to several DOFs, different values can be set in different directions. Furthermore, boundary conditions can be assigned to connector elements, such as controlled displacement or velocity.

In Figure 3.1b an example of a cartesian connector element is illustrated in two dimensions. The connector element is defined in a local coordinate system (x',y') that follows node A and has been given the attributes; linear elasticity $k_{x'}$ in x' -direction and linear damping $c_{y'}$ in y' -direction. The fixed ends of the spring and dashpot are fixed in the (x',y') -coordinate. Hence forces are only applied on node B when B moves relative A in the (x',y') -coordinate system.

Connector elements are elements in the same sense as solid elements and structural elements and hence, reaction loads and stresses can be extracted from them. However, they are implemented making use of Lagrangian multipliers [12]. Consequently, additional variables are added to the system and the size of it is increased.

Connector elements without assigned attributes can be used to take measurements in the model. The measures can be given in the global coordinate system or a coordinate system local to the connector element.

3.4 Constraints

In the finite element formulation a constraint is used to restrict the motion of a DOF. Either the constraint can be a prescribed value, or it can be a prescribed relationship to another DOF. These are usually referred to as *single-point* constraint and *multi-point* constraints, respectively [5]. Furthermore, constraints can be linear or non-linear.

A multi-point constraint involves at least two DOFs, where one is considered the *master* and the remaining DOFs are considered *slaves*. The typical example is the *coupling constraint*. The coupling constraints can be categorised as *kinetic* or *distributing*. In a kinetic coupling, each slave DOF is individually constrained to the master DOF. A distributing coupling constrains the slave DOFs to the master DOF in an averaging sense, such that a weighted average of the slave DOFs' displacements equals the displacement of the master DOF.

Another type of multi-point constraint is the *tie constraint*. It does not have a master DOF but a master surface and a slave surface. Each slave DOF is locked to a position given by the closest master DOFs [13]. It can be thought of as the two surfaces are “glued” to each other.

Different methods can be used to set up a constraint. In a commercial software such as Abaqus[®] a common approach is to make use of a graphical interface. The constrained DOFs are associated with either a set of nodes or a surface. The software associates the surface or set of nodes with a set of DOFs to which the constraint applies. This is a very useful method that allows the mesh to be regenerated or refined without the need to redefine the constraints.

3.5 Contact Interactions

Contact interactions are used to model physical contact between parts that cannot be modelled with constraints. For example when contact between two parts is initiated at a beforehand unknown time during a dynamic simulation, or when friction is present in a contact. A *node-to-surface* contact interaction has a master surface and a set of slave nodes [13] which are not allowed to penetrate the master surface.

An interaction works in “two directions”, the normal direction and the tangential direction. A distance, or *clearance*, is allowed between the parts in the normal direction. As long as the clearance is larger than zero, the contact is inactive. In each solver iteration, the clearance is measured and the contact is activated when the clearance becomes negative. A negative clearance is called *overclosure*. This activates a reaction force in terms of a contact pressure with magnitude depending on the size of the contact surface area and the overclosure [14].

It is possible to model the normal behaviour in different ways [14]. If modelled as a *hard contact*, the contact pressure is zero as long as the overclosure is zero. When

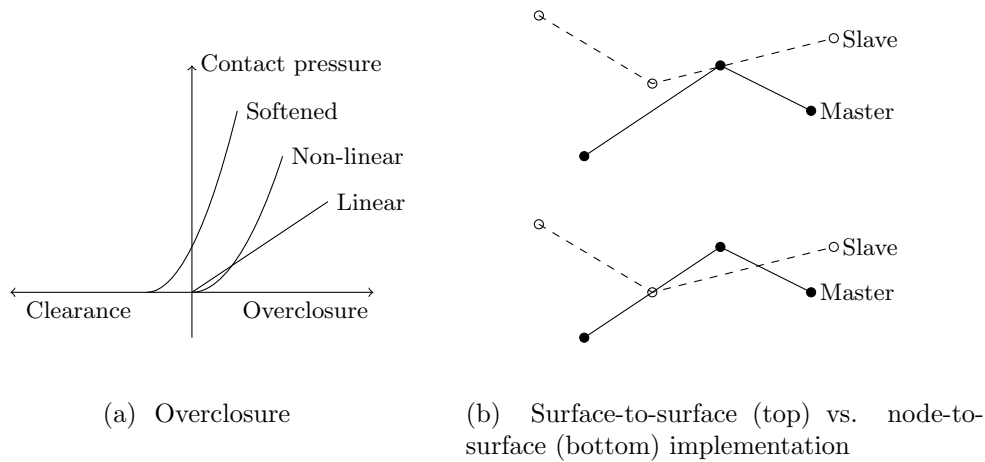


Figure 3.2: Contact characteristics. Based on figures in [14] and [13].

an overclosure is detected, a contact pressure is calculated for the next iteration. Lagrangian multipliers can be utilised to calculate the contact pressure in order to obtain a minimal overclosure. However, a more numerically stable method is to calculate the contact pressure as a penalty based on the overclosure. In its simplest form, the contact pressure is calculated as a linear function of the overclosure but non-linear models may also be used. It is also possible to “soften” the contact in order to obtain a more stable solution or to model surfaces where actual softening is present, such as surface coating. A soften contact is implemented similar to the penalty method, with the exception that the contact pressure is not identically zero for a small clearance. The different penalty models are illustrated in Figure 3.2a.

In the tangential direction a friction dependent contact interaction can be implemented. Commonly, the friction force is linearly related to the normal force via the friction coefficient, μ , but also non-linear behaviour is possible to implement. Analogously to the normal direction behaviour, the friction force is inactive until the two surfaces are in contact with each other.

As mentioned above, a contact can be implemented as a master surface and a set of slave nodes, called node-to-surface implementation [8]. Contact is considered initialised when a slave node penetrates the master surface. At the bottom of Figure 3.2b a node-to-surface implementation is illustrated. As can be seen, a convex master surface is allowed to penetrate the slave surface without activating the contact and an error is introduced. The errors due to how contact is modelled can be reduced by a proper choice of master surface. If one surface is larger than the other, the larger surface should be taken as master. Otherwise there is a risk that the slave surface “wraps” around the edge of the master surface. If the parts that are in contact are of different materials, it is desirable to have the stiffer part as master. If the meshes are not equally fine, the surface with the coarser mesh should be chosen as master surface [13].

A more sophisticated implementation is the *surface-to-surface* implementation, shown at the top in Figure 3.2b [13]. In this approach, the slave surface is interpo-

lated between the nodes which gives a more accurate contact representation. Also, the contact pressure is calculated in an average sense which gives a smoother representation of the contact pressure over the contact surface. Additionally, smoothing algorithms can be used on cylindrical and spherical surfaces to better capture the geometry.

3.6 Substructures

A substructure, also known as “superelement”, is a part for which a number of DOFs have been reduced through an elimination process, for example by performing a Gauss elimination, but stopping before the stiffness matrix is entirely reduced [5]. Only a subset of DOFs are retained in order for the substructure to interact with the other parts or to apply boundary conditions or loads.

In the simulation where the substructure is included it can be thought of as a single solid element, or a set of (retained) DOFs where each DOF has mass-, damping- and stiffness properties. Substructuring can be very useful when investigating various designs that should fit in a specified interface [6]. The retained DOFs can be kept the same while the design is altered, resulting in stiffness variations of the retained DOFs.

Consider the structure illustrated in Figure 3.3 (1) as an example. It consists of two instances of a square shaped part that can be assembled, meshed and simulated as usual, shown in Figure 3.3 (2). Assuming each node has two DOFs, there are in total 164 free DOFs. However, instead of conducting the simulation on an assembly of solid part instances, the part can be turned into a substructure before it is included in the assembly. In Figure 3.3 (3) the solid part instances are identified and in Figure 3.3 (4) they are replaced with substructures.

Here the DOFs on the upper and lower surface of the part (marked with dots in Figure 3.3 (4)) are retained since they interact with the ground or the other instance or have loads assigned to them. All information about the part (mass, stiffness and damping) is stored in the retained nodes which implies that in Figure 3.3 (5) the substructures are assembled into a system with a total of only 14 free DOFs. Furthermore, assume that the design is part of a larger context; then it is possible to redesign the interior of the part but keep the design of the upper and lower surface and generate a new substructure with the same retained DOFs. Hence the DOFs in the system are kept the same, only the response varies.

The displacement vector, $\mathbf{U} \in \mathbb{R}^N$ is reduced to $\mathbf{U}^{\text{Ret}} \in \mathbb{R}^{N^{\text{Ret}}}$ where N is the number of DOFs for the part and N^{Ret} is the number of retained DOFs, $N^{\text{Ret}} < N$. Further, the size of the mass-, damping- and stiffness matrices are reduced from $\mathbb{R}^{N \times N}$ to $\mathbb{R}^{N^{\text{Ret}} \times N^{\text{Ret}}}$. If the load and displacement condition for the substructure is known or can be approximated beforehand, the substructure can be generated pre-loaded.

There is a linear transformation, $\mathbf{L} \in \mathbb{R}^{N \times N^{\text{Ret}}}$, which relates the set of retained field variables and the field variables for the entire part such that the response of

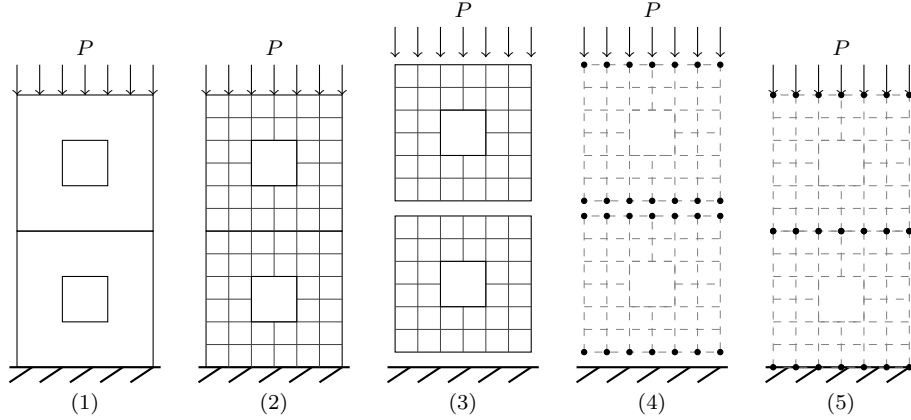


Figure 3.3: Substructuring illustrated in five steps.

the part is given by [14]

$$\mathbf{U} = \mathbf{U}_0 + \mathbf{L}\Delta\mathbf{U}^{\text{Ret}}. \quad (3.3)$$

where \mathbf{U}_0 contains the displacements of the preloaded structure and $\Delta\mathbf{U}^{\text{Ret}}$ contains the retained DOFs' deviations from the preloaded state. Hence, given that the displacements for the retained DOFs are known it is possible to recover the displacements for all DOFs. The response of the substructure is then given by a linear perturbation around the state at which the substructure is generated. Note that the substructure must be in equilibrium when it is generated, such that the substructure's contribution to the overall equilibrium of the model is given by the linear response only [14].

3.7 Material Model

This section is a brief summary of the material model used for the FE-modelling in Abaqus[®]. For a thorough theory, the reader is referred to the Abaqus Theory Guide [14].

In one dimension, the engineering strain is defined as the change in length, Δl , divided by the original length, l_0 , as: $\epsilon^{\text{Eng}} = \Delta l/l_0$. The true strain, ϵ , is defined as the sum of all engineering strains, given by

$$\epsilon = \int_{l_0}^{l_f} \frac{dl}{l} = \ln\left(\frac{l_f}{l_0}\right) \quad (3.4)$$

where l_f is the final length after the loading process is finished. Similarly, the engineering stress is the force, F , divided by the original cross section area, A_0 ; $\sigma^{\text{Eng}} = F/A_0$ while the true stress is defined as the force divided by the instantaneous area, A , as

$$\sigma = \frac{F}{A}. \quad (3.5)$$

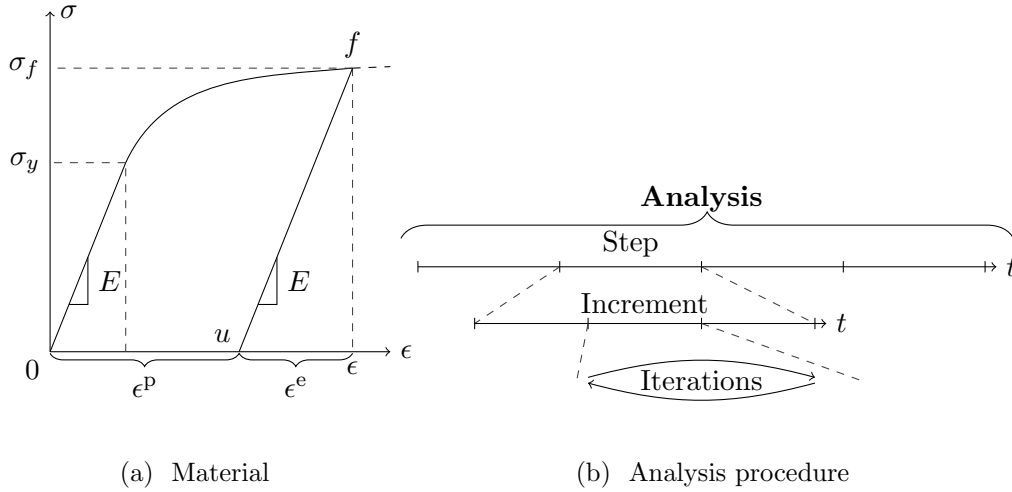


Figure 3.4: Illustration of the isotropic elastic–plastic material model in (a). Illustration of the relations between *Steps*, *Increments* and *Iterations* in (b).

In an isotropic elastic–plastic material model, the relation between the true strain, ϵ , the elastic true strain, ϵ^e and the plastic true strain, ϵ^p , is given by

$$\epsilon = \epsilon^e + \epsilon^p = \frac{\sigma}{E} + \epsilon^p \quad (3.6)$$

where σ is the true stress and E is Young’s modulus. The plastic strain relates to the stress with a possibly non-linear relation $\epsilon^p = \epsilon^p(\sigma)$, commonly implemented in the FE-model as tabular data determined by experiments. This is illustrated in the hysteresis curve in Figure 3.4a.

The origin corresponds to an unloaded structure. When a load is applied to the structure, the response is linear with the stress up to a certain point, $\sigma = \sigma_y$, at which the material starts to plasticise and the plastic strain is introduced. The loading continue until the point f is reached. When the material is unloaded, the stress goes back to zero while the strain is not. The plastic strain remains as a permanent deformation, as can be seen at the point u in Figure 3.4a.

Isotropic hardening means that the yield surface increases uniformly in all directions when the yield stress, σ_y , is exceeded. Hence, if the material is unloaded and again reloaded, the yield limit is increased regardless of the direction of the reloading. If the structure which response is described with the curve in Figure 3.4a is again loaded, the response is linear as long as the stress does not exceed σ_f , which is the increased yield limit. If σ_f is exceeded, the response continuous along the dashed curve from f onwards.

3.8 Solver Procedure

A simulation, or an analysis, in Abaqus[®] is divided into several consecutive *steps*. By default there is an initial step in which the model is first defined but no loads

can be applied in this step. There are various types of steps available for different types of analyses, such as static implicit, dynamic implicit, substructure generation or frequency analysis [10]. Also, static analysis steps can be followed by dynamic analysis steps and vice versa. The analysis partitioning is illustrated in Figure 3.4b.

The frequency analysis (eigenvalue calculation) and the substructure generation steps are so called *linear perturbation steps*. That is, the calculations performed in the step is a linear perturbation around the final state in the previous step. The static implicit and dynamic implicit steps on the other hand, affects the model and recalculates its state with respect to the loads and boundary conditions in the current step and uses the previous step as initial condition. These are called *general steps*.

Both the static and dynamic implicit steps have a defined time scale, although the static implicit analysis does not account for velocity and acceleration effects. In a static analysis, the time scale is used to ramp up the loads, also known as load stepping. In a dynamic analysis the time scale defines the magnitudes of the acceleration and velocity in the model. For these purposes each step is divided into several *increments*. By default the number of increments is unknown beforehand since Abaqus[®] automatically adjusts the size of the increments depending on the progress of the solution. In each increment, a solution of the equation system is found implicitly using Newton's method [10]. This is denoted as *iterations* in Figure 3.4b. If a converged solution is not found within a certain number of iterations, a new attempt is made with a smaller increment size.

For problems that undergo large deformations, the matrices in equation (3.1) have to be recalculated for each increment. Simple linear static problems where small deformations can be assumed can on the other hand be solved in one increment and one iteration.

Section 4

FE-model Implementation

In this section, a thorough description of the FE-model implementation is given. Three different models are presented, utilising different methods for the implementation of the reaction plates and the level of simplification. Boundary conditions, loads and added springs and dampers are described and motivated and a base load case is defined.

The section continues with a discussion on the results from pre-analyses conducted to determine settings for the model implementation. It is finalised with an investigation of the convergence status of the suggested mesh settings.

4.1 Connector Elements Model

The connector elements model, illustrated in Figure 4.2, is a simplified model of the HCS-R system. The motion of the model is restricted to be symmetric in the x - z -plane¹. Hence utilising symmetry boundary conditions, only one half of the structure has to be modelled. This reduces the variety of load cases that can be simulated but also reduces the computation cost as compared with a full model.

Parts that are subject to contact interaction are modelled as solids. This includes: the rod and funnel, the inboard and outboard hubs, two parts to simulate the contact between the termination and porch reaction plates. The termination support is modelled as a solid while the landing frame is modelled as a rigid analytical surface. Note that the hubs have been modelled partly, such that only the area closest to the contact are included. Also, a piece of the jumper spool is included, modelled with beam elements and a thick walled pipe profile. The inner and outer diameter of the jumper spool profile used for the half model are recalculated such that its axial- and bending stiffness equals that of half the jumper spool for the full model.

An elastic-plastic material model, as described in Section 3.7, *Material Model*, is used for all solid parts. Two different materials (metals) are used, *F65* for the hubs and *S355* for all other parts [3]. The basic properties for the materials are summarised in Table 4.1. In Figure 4.1a and Table 4.1b the plastic strains for the materials are presented in graphical form and in tabular form, respectively.

A thread-model, or a “mass-less rigid body”, is built of rigid connector elements to which the deformable solid parts are connected. The model, with denotations, is illustrated in Figure 4.2. Note that some connector elements are used for measurements only.

¹ x is the stroking direction and z points upwards

Table 4.1: Summary of material properties.

Property	S355	F65
Mass density	7 750 kg/m ³	7 750 kg/m ³
Young's modulus*	200.35 GPa	203.75 GPa
Poisson's ratio	0.31	0.3
σ_y^*	323 MPa	447 MPa

* At 0°C and 0.2% plastic strain.

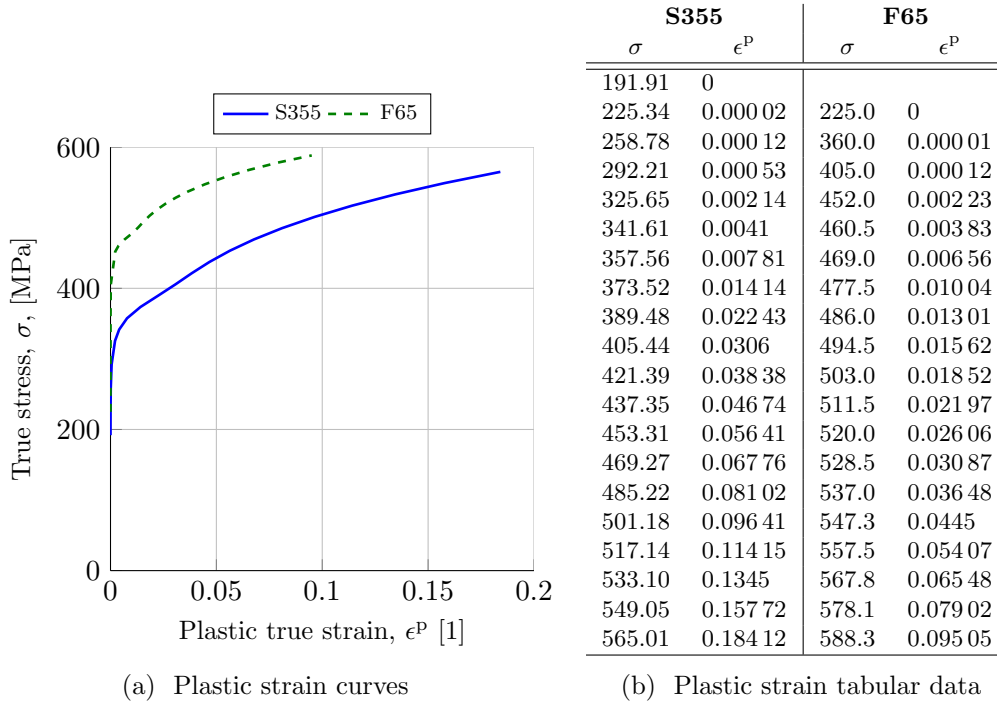


Figure 4.1 & Table 4.2: Plastic strains.

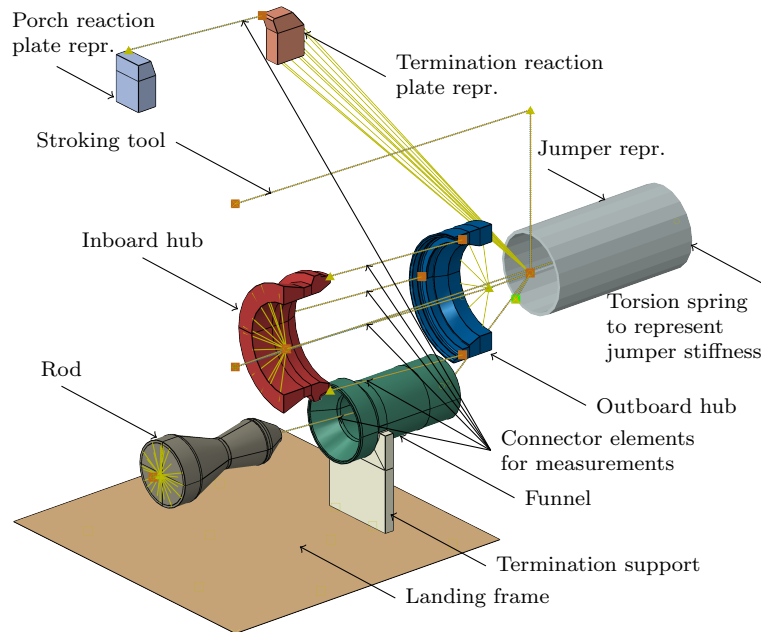


Figure 4.2: The simplified connector elements model, with connector elements and constraints illustrated.

To represent the mass and rotary inertia of the termination a point inertia element is located at the termination’s center of gravity². The assumed mass of the termination is³ 2 000 kg. Similar, a mass element representing the jumper weight is located at the point where the jumper connects to the termination. The mass of jumper is assumed to be⁴ 25 000 kg, of which a quarter is supported by the half model.

4.1.1 Connections, Constraints and Contacts

Connections between parts are created in two steps. First, the DOFs at the surface are constrained to a reference point⁵ using a kinematic or distributing coupling constraint. For the rod and funnel, which are welded to the termination and porch reaction plates, respectively, kinematic couplings are used. Distributing couplings connect the hubs and the thread model in order not to “lock” the hubs cross-sections. Second, connector elements are used to generate the rigid connections between the reference points. A combined connector element–constraint connection of the rod to a reference point is depicted in Figure 4.3a. Also a local coordinate system in which the connector element is defined is illustrated.

²The actual center of gravity is not located in the symmetry plane, but was assumed to be so for the half models.

³The values for the mass and inertia of the termination and its center of mass were obtained from a CAD model of the termination.

⁴Value based on the mass for a “normal jumper spool” [3].

⁵Both the Abaqus[®] features *Attachment Point* and *Reference Point* were used.

The stroking tool is modelled with an axial connector element with an initially fixed length implemented between two reference points as illustrated in Figure 4.2. The rigid connector elements used to connect the rod, funnel, hubs and jumper to the termination and porch⁶ are used to measure reaction loads in these parts. Cartesian- and rotation connector elements without assigned attributes are used to measure distances and tilt angle between the termination and the porch at various locations.

The part at the termination reaction plate that interacts with the porch reaction plate is connected to the center of the termination thread model with a kinematic coupling constraint. The constraints are visualised in yellow in Figure 4.2.

Surface-to-surface contact interactions are used to simulate the contacts in the structure. In Figure 4.3b the surfaces involved in contact interactions have been coloured blue. There are in total four contact interactions, here listed with the chosen master surface first; landing frame to termination support, funnel to rod, outboard hub to inboard hub and porch reaction plate to termination reaction plate. The last contact is only defined for the small solid parts included in the model to represent this particular contact.

In the normal direction, a linear penalty with default stiffness is implemented. The tangential contact is modelled using friction coefficient μ_1 for all contacts except the landing frame to termination support contact where a larger value, μ_2 , is used. Different values are used since the landing frame surface is painted while the other surfaces are processed to certain degrees of roughness and also treated with friction reducer. Abaqus[®] automatic surface smoothing, capable of smoothing axisymmetric surfaces, is used where applicable [13].

4.1.2 Boundary Conditions

The porch is modelled as fixed in space. Hence *encastre boundary conditions*⁷ are applied to each part separately, fixing its location in space. Also the surface representing the landing frame is fixed in space with an encastre boundary condition. The inboard hub intersects the x - z -plane and is therefore assigned a symmetry boundary condition.

The parts on the termination side that intersects the x - z -plane⁸ are all subject to a symmetry boundary conditions in the x - z -plane. The condition is implemented on all nodes of the jumper representation, on the symmetry surface of the hub and on one node of the rigid thread model. This implies that all nodes in the rigid thread model are subject to the symmetry boundary condition.

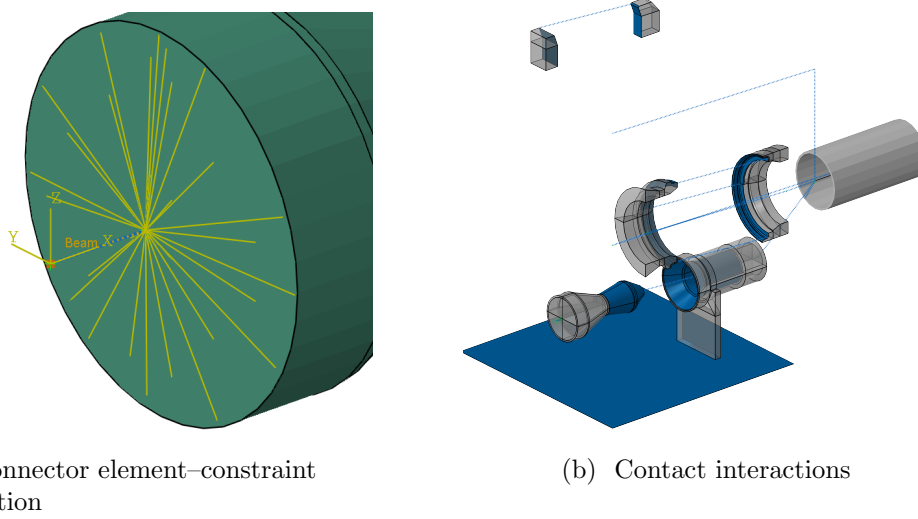
4.1.3 Springs and Dampers

In the x - and z -direction, the termination is supported by contact with the landing frame, the connector element representing the stroking tool and springs attached to

⁶The porch is modelled with boundary conditions.

⁷ $u_1, \dots, u_6 = 0$ for all nodes in the BC, also known as clamped boundary conditions or fixed boundary conditions.

⁸Outboard hub, jumper spool representation and the tread model.



(a) Connector element–constraint connection

(b) Contact interactions

Figure 4.3: Illustration of combined connector element–constraint connection on rod in (a). The connector elements model with surfaces subject to contacts coloured blue in (b).

the end of the jumper spool representation. These springs are implemented through a combined cartesian–rotation connector element attached to a fix point in one end and the rearmost end of the jumper in the other end. The connector element is given the elastic properties: axial stiffness, k_x , and rotational stiffness around an axis normal to the symmetry plane, κ_y . k_x contributes to the back-tension while κ_y times an initial tilt angle gives the expected bending moment in the jumper at the end of the stroke. Later on, load cases are defined in which both the jumper spool stiffness and the tilt angle are altered.

Between the funnel and rod, a connector element with linear damping property, c , is placed. Convergence issues were experienced during early tests when the funnel-to-rod contact reaches the thickest section of the rod. An abrupt decrease in the axial reaction force generated by the friction between the funnel and rod with large accelerations and instability as result was found to be the cause. A velocity dependent damper is therefore introduced to reduce the velocity at this point. The magnitude of c is kept small enough for the damper force to be insignificant at normal stroking velocity, but large enough to damp the motion when the friction reaction force is reduced and the velocity increased.

4.1.4 Loads

The axial force, or back-tension, acting on the termination in positive x -direction, F^{BT} , is modelled as

$$F^{\text{BT}} = k_x \cdot x + F_{\text{Const}}^{\text{BT}} \quad (4.1)$$

where k_x is the stiffness of the spring representing the axial stiffness of the jumper spool, x is the stretch distance of the spring and $F_{\text{Const}}^{\text{BT}}$ is a constant force. Modelling

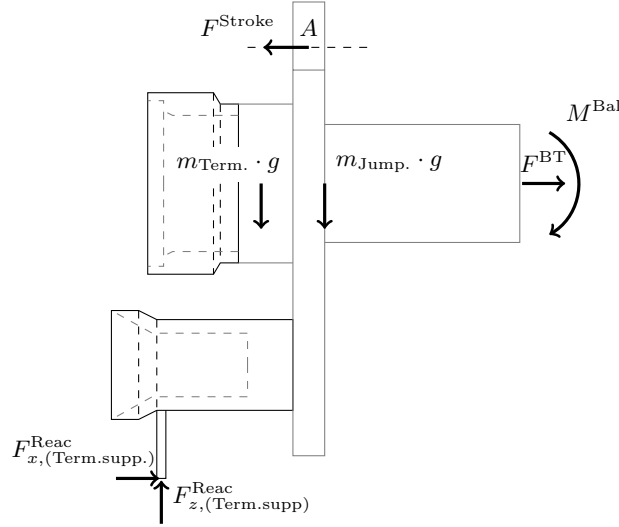


Figure 4.4: Schematic illustration of the loads acting on the termination at the initial position.

F^{BT} in this way makes it possible to simulate a load case with an initially unloaded jumper spool ($F_{\text{Const}}^{\text{BT}} = 0$) as well as a jumper spool subject to a constant back-tension ($k_x = 0$). F^{BT} represents the back-tension acting on the full model and is therefore divided by two for the implementation of the half models.

At the initial position, the termination must be in force and moment equilibrium. The exterior forces acting on a simplified two dimensional model of the termination are illustrated in Figure 4.4. Significant forces in axial (x -) direction are: force from stroking tool, F^{Stroke} , friction force on the termination support, $F_{x, (\text{Term.supp.})}^{\text{Reac}}$, and back-tension in jumper, F^{BT} . In the vertical (z -) direction, the significant forces are: gravitational force, $m_{\text{Term.}} \cdot g$, reaction force on termination support, $F_{z, (\text{Term.supp.})}^{\text{Reac}}$, and shear force from jumper, $m_{\text{Jump.}} \cdot g$, (here assumed to equal the gravitational acceleration times the mass of the jumper supported by the termination). Force equilibrium is guaranteed due to the geometry and the boundary conditions, but moment equilibrium is not. Therefore, moment equilibrium has to be ensured manually.

When the termination is placed on the landing frame, the combination of forces and the locations at which they act may cause the termination to rotate around the y -axis which in turn generates a reaction moment in the jumper spool. The moment is transmitted to the termination which attains a tilt angle at which it balance itself with respect to moment equilibrium. In the simulations, it is desirable to be able to control the initial tilt angle. This can be achieved by introducing a balancing moment applied at the end of the jumper representation.

The magnitude of the balancing moment can be calculated from moment equilibrium around the point to which the stroking tool force acts, A in the figure. Thus the only unknowns are the balancing moment and the axial reaction force due to friction between the landing frame and the termination support. To minimise the

deformation and misalignment of the termination and increase the control of the initial position, the frictional force can be assumed to be zero initially. That is, the termination is in perfect moment equilibrium without the need to introduce the frictional force. Note that this does not affect the simulation in any other way since the frictional force will be initialised as soon as termination is moved from its equilibrium state. Further, the same balancing moment is used for all initial tilt angles why the friction force initially may not equal zero exactly. In addition, deformations of the termination change the geometry and thereby slightly affect the moment equilibrium.

4.1.5 Steps

The simulation is conducted in three *Steps*⁹. The purpose of the first two steps is to place the termination into position on the landing frame and to initialise the reaction forces required to hold the termination in this position. Since the termination already is in contact with the landing frame, but unloaded, static analyses can be used in the first two steps. The third step is the stroking where an implicit dynamic analysis is implemented.

In addition to the boundary conditions described above, the bottom of the termination support is initially fixed in x - and y -direction which makes the friction force between the landing frame and the termination support redundant at first. In Step 1, the loads and the contact between the termination support and the landing frame are initialised. However, the bottom of the termination support is still fixed in x - and y -direction to better control the positioning of the termination. At the end of Step 1, the termination is deformed due to the gravity load and there is a contact pressure between the landing frame and termination support. The boundary condition on the bottom of the termination support is inactivated in Step 2, introducing the friction force between the landing frame and the termination support. At this stage, the termination is in rest with its entire weight supported by the landing frame.

In Step 3, the connector element representing the stroking tool is shortened through a controlled deformation. This pulls the termination against the porch. A constant stroking velocity throughout the step and a specified time span for the step gives control of the total stroking distance.

4.1.6 Base Load Case

A load case is defined as a certain combination of position, parameter settings and applied loads. Below are the settings for the base load case described¹⁰.

The termination is aligned with the porch but translated 500 mm in x -direction and 35 mm in negative z -direction from its *assumed final position*. The assumed

⁹In Abaqus[®] the problem history is divided into steps, where each step is a convenient phase of the history. See Section 3.8, *Solver Procedure*.

¹⁰See Section 4.6, *Pre-simulations* for further motivations and discussion of the the settings chosen for the base load case.

final position is defined as: the position of the unloaded termination when the hub-faces¹¹ are in contact. It is worth to stress that the termination will not end up in the assumed final position for any load case since it is subject to loads and hence deformed at the end of the stroke. The purpose of introducing the assumed final position is to be able to compare the load cases and evaluate whether or not the stroking for a load case is accepted.

Two friction coefficients are used; $\mu_2 = 0.2$ for the contact between the funnel support and the landing frame and $\mu_1 = 0.12$ for all other contacts. The values represent common values used for the specified types of contacts. It was taken into account that the surfaces interacting in the contact between the landing frame and the termination support are not processed in the same way as the other contact surfaces.

The elastic properties for the connector element representing the jumper stiffness are given the values: $\kappa_y = \kappa^{\text{Base}}$ kNm/deg and $k_x = 0$ kN/mm. κ_y is chosen to represent approximately $M_{\text{upper}}^{\text{Test}}/2$ kNm at a $\alpha_{y,s}$ deg misalignment. According to a previous test report of a similar system, the HCS-R moment capacity for initial backward tilt is approximately $M_y = M_{\text{upper}}^{\text{Test}}$ kNm [1]. Half this value for a moderate tilt angle is considered reasonable for the base load case. The magnitude of the modelled back-tension is set to the constant value 100 kN, also based on values used in the previous test. Note that the values presented here for k_x and κ_y represent values for the full model, hence only half the values were implemented in the half models.

4.2 Substructures Model

In order to account for the response of the porch- and termination reaction plates in the model, the rigid connector elements connecting the solid parts in the connector elements model are replaced with substructure representations of the reaction plates. The use of substructures reduce the number of elements and nodes in the model compared with a model with only solid parts which imply that less calculations have to be performed.

The substructures model of the HCS-R system is depicted in Figure 4.5a. The model is coloured by element integration order where red means reduced integration (first order) and white means full integration (second order). The red transparent parts are the substructures and the green part is a rendering of the beam elements in the jumper representation.

The substructures are modelled and generated in separate analyses and imported to the FE-model of the HCS-system as separate parts. Only a small number of DOFs are retained in order to reduce the size of the model as much as possible. The retained nodes on the porch are; the attachment point for the inboard hub, for the rod, for the stroking tool and for the boundary conditions. The nodes from which DOFs are retained are marked red in Figures 4.5b and 4.5c. Note that only

¹¹The hub face has normal vector aligned with the hub's symmetry axis and pointing towards the other hub. In the assumed final position the hub faces are parallel and connected with only a thin rubber between them.

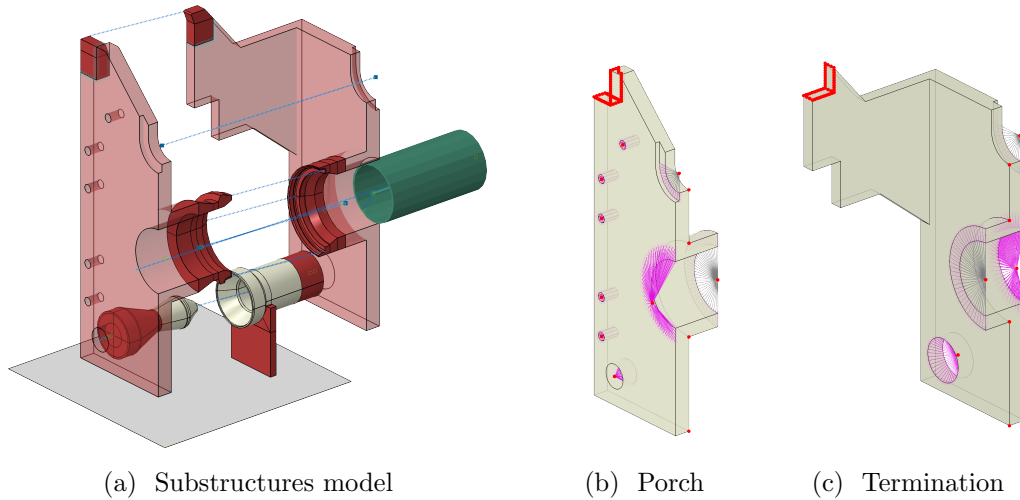


Figure 4.5: The substructures model in (a), coloured by element integration order. Reduced integration (first order) is used in red areas while full integration (second order) is used in white areas. Red transparent parts are the substructures and the green part is a rendering of the beam elements in the jumper representation. In (b) and (c) are the porch- and termination reaction plate substructure, respectively. Nodes from which DOFs are retained are marked red.

a small number of nodes are retained on the symmetry plane, hence the symmetry condition is only satisfied approximatively. Also, several of the retained nodes do not lie on the actual part but are centre points of holes or slots. The constraints used to constrain these nodes to the part are implemented in the separate analyses for the substructure generation.

The stroking tool is again represented by an axial connector element implemented between two reference points. Distributing couplings are used to constrain the reference points to the porch and termination slots. Also the hubs are connected to the porch and termination substructures via distributing couplings and connector elements. Similar approaches are used for the jumper, rod and funnel with the exception that kinematic couplings are used. The small solid parts used to model the contact between the reaction plates are connected to the substructures through a node-to-surface tie coupling between the solid parts and a set of retained nodes on the substructure.

The symmetry boundary condition is implemented on a set of retained nodes in the symmetry plane, visible in Figure 4.5b and Figure 4.5c. The clamp boundary condition on the porch is applied to a set of six retained nodes on the porch substructure; the centres of the five bolt holes with which the porch is fixed to the subsea structure and the rearmost centre point of the inboard hub. Kinematic constraints are used to constrain these nodes to the porch reaction plate substructure.

The base load case can be applied to the substructures model without any modifications.

4.3 Solid Parts Model

The solid parts model is implemented analogously with the substructures model except that the reaction plates are modelled with solid parts instead of substructures. Constraints and connector elements are used to connect the solid parts in the same way as for the connector elements model and the substructures model. To model the symmetry boundary condition, all nodes on the surfaces of the reaction plates that intersect with the x - z -plane are chosen. Hence the symmetry condition is satisfied to the maximum possible accuracy for the given element discretisation.

4.4 Elements for Solid Parts

All solid parts are meshed using eight nodes linear hexahedron elements (“linear brick elements”) with reduced integration, except for some areas where hourglassing were encountered in the pre-simulations, coloured white in Figure 4.5a. This is to avoid shear locking and volumetric locking and to keep the computational cost down. In the areas where hourglassing was seen, second order integration elements are used. The jumper spool representation is modelled with linear beam elements.

Several factors are taken into account when choosing element type. The decision is supported by the following arguments:

- It is the most common element type used within AKS.
- Elements of low order requires, in general, less computations. First order tetrahedron elements model the stress as constant within the element and are overly stiff, hence they should be avoided if possible [12].
- Well structured meshes can be generated with hexahedron elements. The element boundaries can be aligned with load directions at contacts which gives better convergence properties.
- It is considered the best compromise between computation cost and accuracy. A good hexahedron element mesh for a general analysis usually provides the same accuracy as a tetrahedron mesh but to a lower cost [12].
- The element type is known to produce good results where contacts are involved [13].
- The bending deformations are considered small why there should not be a problem that the element type does not handle bending very well [12].

4.5 Definitions

Reaction forces, $F_{(x,z)}^{\text{Reac}}$, reaction moments, M_y^{Reac} , relative positions, $d_{(x,z)}^{\text{Rel}}$, and tilt, α_y , are measured at numerous locations in the models. Figure 4.6 depicts a schematic illustration of locations and directions of relative position measurements and reaction loads for a half model. The reaction force measured in the stroking tool is denoted

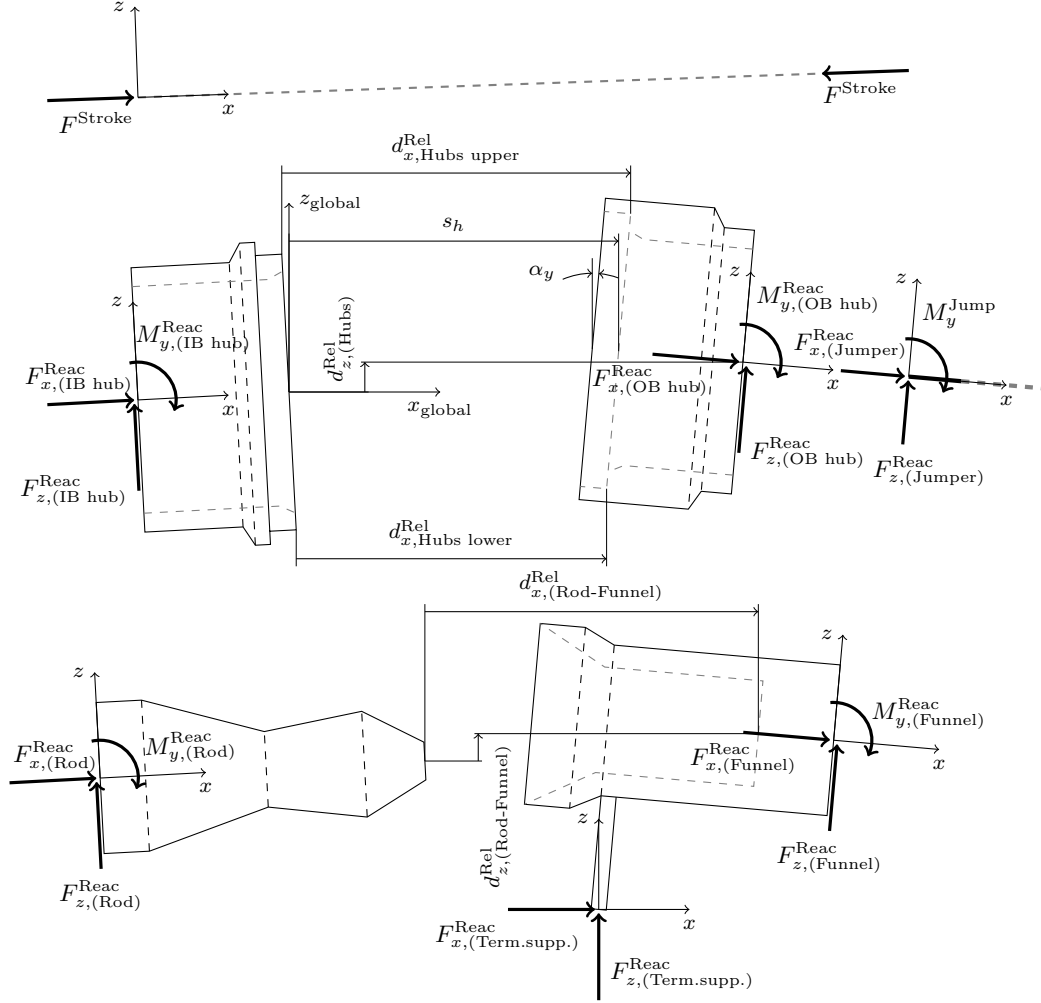


Figure 4.6: Directions and locations of the relative positions and definitions of reaction loads. Inboard hub and rod to the left, outboard hub, funnel and termination support to the right. Note that the figure is not to scale.

F^{Stroke} and shall be considered as the stroking force that need to be applied to the system in order to achieve the desired displacement. It acts on the termination's slot and is defined as positive when directed towards the porch's slot, cf. Figure 2.1. Similarly, the reaction moment (in y -direction) measured where the jumper connects to the termination is denoted M_y^{Jump} .

The measures of relative positions, tilt and angular misalignment are defined in the global coordinate system. The reaction plate representations are not included in the figure. However, the relative position of the reaction plates representations are measured similar to the relative positions for the rod and funnel and for the hubs. Furthermore, all relative positions are zero in the assumed final position. The global coordinate system is positioned such that x is aligned with the stroking direction pointing from the porch towards the termination, z points upwards and y fulfils a

Table 4.3: Four models for pre-simulation.

Model	Stroke velocity	Material implementation	Rod-to-funnel damper
1	25 mm/s	Elastic-plastic	0.1 kNs/mm
2	12.5 mm/s	Elastic-plastic	0.1 kNs/mm
3	25 mm/s	Linear elastic	0.1 kNs/mm
4	25 mm/s	Elastic-plastic	0 kNs/mm

right handed coordinate system.

The reaction forces and reaction moments are defined in the coordinate system local to their associated connector element and as they are felt by the individual parts. Thus reaction forces and moment are always defined in the same directions with respect to the part they are associated with. For small angular deformations, the local systems coincide approximately with the global system. The reaction forces in the jumper and the jumper moment are measured such that they represent the loads from the jumper felt by the termination. Hence the jumper moment, M_y^{Jumper} , includes both the reaction moment due to tilt and the balancing moment. At the end of the jumper spool representation (not illustrated), the jumper back-tension, F^{BT} , acts in the global x -direction.

The distance between the current position and the assumed final position, measured at the hub's centres, is denoted s_h in Figure 4.6. This measure is used as scale on the x -axis for the majority of the graphs in Section 5, *Results*. For the base case, in which the initial position of the termination is translated 500 mm in x -direction and 35 mm in negative z -direction from its final position, the distance between the hubs' centres is $s_h = \sqrt{500^2 + 35^2} \approx 501$ mm. Note that the assumed final position may not be reached exactly due to deformations in the model.

Where nothing else is stated, the distance data is shown unprocessed while the force and moment data are filtered through a second order Butterworth lowpass filter [4]. The coefficients for the filter are chosen manually and differs from plot to plot.

4.6 Pre-simulations

The model settings have been evaluated to ensure that the model is stable and capable of simulating numerous load cases. Pre-simulations were conducted on the connector elements model with altered settings. In Figures 4.8, 4.9 and 4.10 three output data for four different models are compared for the last 200 mm of stroke. These are referred to in the following discussion. The models differ on a few points, as described in Table 4.3.

4.6.1 Static vs. Dynamic Simulation

The stroking procedure is a rather slow process; stroking the termination the 500 mm from its initial position on the landing frame to the final position with the hubs con-

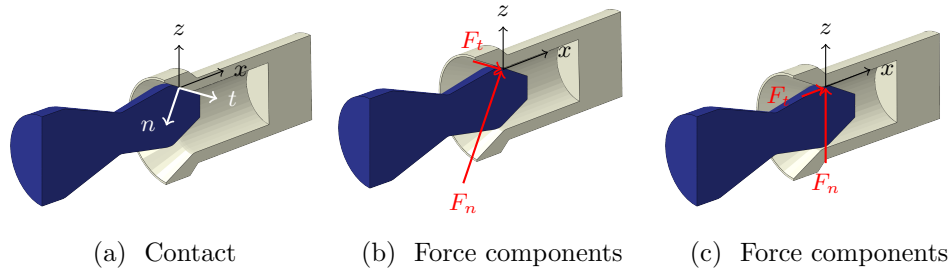


Figure 4.7: Critical rod-to-funnel contact.

nected might take several minutes. The dynamic effects are small and the structure can be assumed to be in static force and moment equilibrium at all times. A *static analysis* is therefore proposed.

In this sense a static analysis can be thought of as if the path for the stroking is divided into small steps and static equilibrium is required in each step. The time dependent terms in equation (3.1) becomes zero and it reduces to $\mathbf{K}\mathbf{U} = \mathbf{P}$. However, from a simulation point of view, the pre-simulations indicate a critical point for the dynamic behaviour of the system when the rod-to-funnel contact reaches the largest diameter of the rod, as illustrated in Figure 4.7.

The design of the rod and funnel implies that the normal and tangential directions of the funnel's contact surface is initially directed as in Figure 4.7a. Consequently, both the normal force and the friction force contribute to the x -component of the force from the rod to the funnel, see Figure 4.7b. At the point when the contact reaches the largest diameter of the rod, the normal direction is aligned with the negative y -direction and only the friction force contributes to the x -component of the rod-to-funnel force as illustrated in Figure 4.7c.

While the funnel moves along the incline of the rod, the termination tilts forward and a reaction moment is built up in the jumper. At the moment the x -component of the rod-to-funnel force is reduced, this reaction moment creates a rotation of the termination back towards its original position. This rotation is problematic to capture in a static analysis. Consequently, the model has to be simulated with a *dynamic analysis*.

The *moderate dissipation* setting in Abaqus[®] is used to control the numerical damping. Typical applications when moderate dissipation is used are: insertion analysis, impact analysis and analyses where high frequency vibrations are incidental. For such simulations, some numerical energy dissipation can improve convergence and reduce noise without significantly reduce the accuracy [10].

4.6.2 Time Frame

The dynamic analysis requires a time frame to be set. That is how long time the stroking procedure will take in the simulation. This time frame affects the velocity and hence the dynamics and the kinetic energy of the model. Different time frames were tried out and compared in terms of the obtained reaction forces and energy levels. As was mentioned above, the stroking procedure may take several minutes.

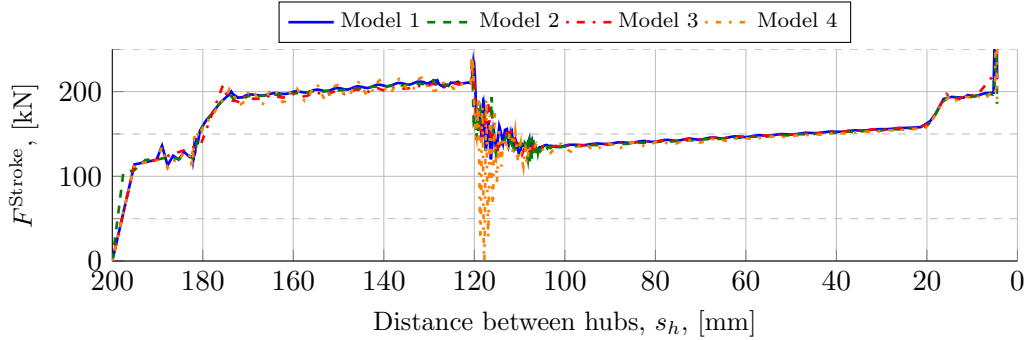


Figure 4.8: Required stroking force, F^{Stroke} , for four different models.

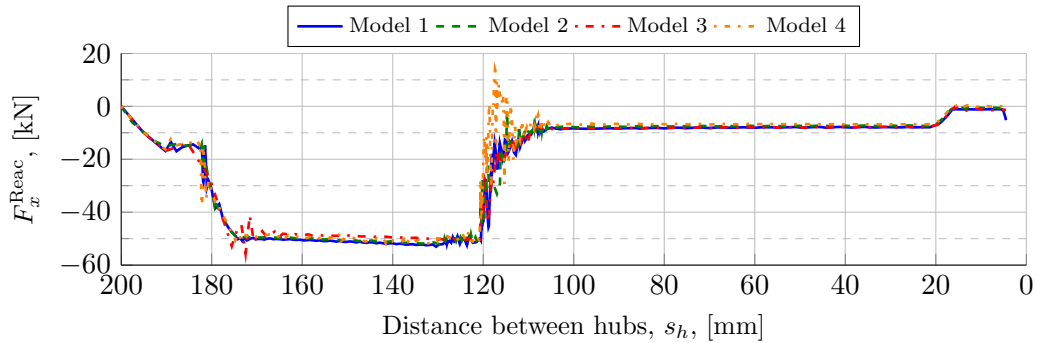


Figure 4.9: Funnel reaction force in (local) x -directions, F_x^{Reac} , for four different models.

However, it turns out that it can be modelled with a significantly shorter time frame while still obtaining the same reaction forces and moments. This actually helps the convergence of the model since a very low velocity makes the model behave more like the model in the static analysis which implies convergence issues.

In Figures 4.8, 4.9 and 4.10 Model 1 and Model 2 have the same settings except for the stroking velocity, which in Model 1 is 25 mm/s and in Model 2 is 12.5 mm/s. It can be seen that the two models show similar behaviour.

Further, the kinetic energy, U_{kin} , can be compared with the energy due to external work, U_{ext} . For a stroking velocity up until $500 \text{ mm}/20 \text{ s} = 25 \text{ mm/s}$, the kinetic energy is less than 1% throughout the entire stroking path expect for some peaks for which the kinetic energy is less than 5%¹². The $U_{\text{kin}}/U_{\text{int}}$ ratio is of the same magnitude as the error in total energy balance in Abaqus[®], which too is kept within about 1% [10].

¹²The numbers are based on a model with an additional damper between the rod and funnel as described in Section 4.6.4, *Stabilising the Model*

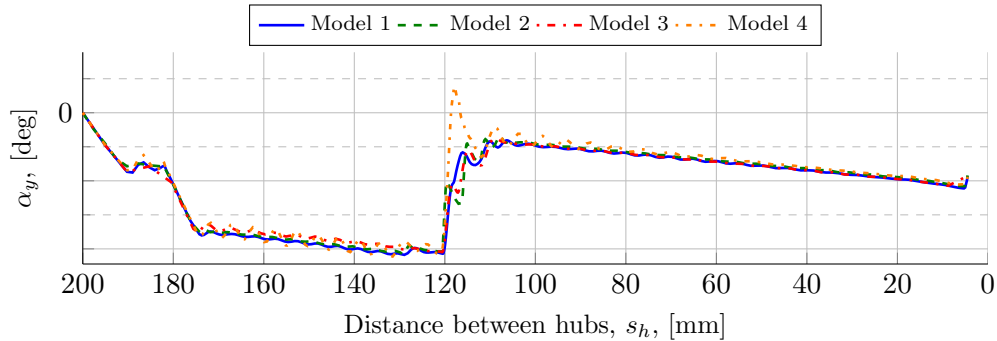


Figure 4.10: Tilt of termination in y -direction, α_y , pre-study. A negative value means tilt forward.

4.6.3 Material Implementation

An elastic–plastic material implementation, described in Section 3.7, *Material Model*, and a linear elastic material model were tried out. Model 3 in Figures 4.8, 4.9 and 4.10 is implemented with linear material properties. As can be seen in all figures, the linear material implementation shows values of slightly less magnitude for all three load curves. Also, additional noise in the funnel reaction force is visible for $s_h \approx 175$ mm. This is where the contact between the rod and funnel is first introduced.

4.6.4 Stabilising the Model

The numerical damping due to the setting of moderate dissipation analysis does not only add very little damping. It turns out that low frequency oscillations of the termination tilt angle appear when the rod and funnel are in contact. The oscillations start at the first impact and are amplified due to the issue with force and moment equilibrium described in Section 4.6.1, *Static vs. Dynamic Simulation*. To reduce these oscillations and stabilise the model a linear damper (cf. dashpot) is modelled between the rod and the funnel, implemented with a connector element. Damping is only set in the global x -direction. The value is chosen to affect the solution as little as possible while still stabilising the model.

Model 4 in Figures 4.8, 4.9 and 4.10 illustrates this. It has the same settings as Model 1 except that it has no damper implemented. It is clear from Figure 4.10 that low frequency oscillations occur for the tilt angle. Further, it can be seen in Figure 4.8 and Figure 4.9 that the noise which is present for $s_h \approx 115$ mm for all four models are of greater magnitude for the model without the added damper element.

4.6.5 Integration Order

Using elements with reduced integration imply a risk for hourglassing, see Section 3.2.1, *Hourglassing*. In Abaqus[®], the risk can be reduced by using hourglass control [12]. However, the hourglass control is not perfect and hourglassing may occur anyway. Hourglassing can be detected by magnifying the displacements in the model

and check for areas that show element behaviour similar to Figure 3.1a. Also, the hourglass control algorithm introduces an artificial strain energy in the model which should be kept as low as possible. As a rule of thumb the model can be accepted as long as the artificial strain energy is less than say 1 % of the strain energy [3].

Problems with too large artificial strain energy and visible hourglassing behaviour was encountered in the rod and funnel. Increasing the order of integration in the element from first order to second order eliminated the problems.

4.6.6 Controlled Displacement vs. Controlled Force

The stroking tool is more or less a hydraulic cylinder. Control of the tool is by the pressure in the cylinder, which in turn gives control of the generated force. Hence it would be reasonable to model the stroking by applying a force between the porch and termination slots. For the real connection system, the stroking progress can be controlled visually and the applied force can be continuously tuned. Something that is not possible in the FE-model.

Instead a predetermined constant or (preferably) ramped stroking force can be applied to the structure. This was tried out but the results were not satisfying. It was not possible to find a generic expression for the force such that the model showed a stable behaviour. Primarily, problems occur when the rod-to-funnel contact reaches the largest diameter of the rod. This point is not reached until a certain magnitude of the stroking force is attained. When the inclined section of the rod ends, the force generates a large acceleration of the termination with uncontrolled behaviour as result. In the physical model this is (at least partly) taken care of automatically since there is a maximum flow velocity to the hydraulic cylinder. A possible way to model such behaviour in the FE-model would be to limit the velocity of the deformation in the connector element representing the connector element by means of for example (non-linear) damping.

For the analyses in this thesis, an optional approach was chosen. The visual control of the stroking progress implies that a constant stroking velocity is a valid assumption. Therefore, the stroking is modelled with a controlled deformation of the connector element representing the stroking tool. A measurable reaction force representing the required stroking force is generated in the connector element. As long as this reaction force is less than the capacity of the stroking tool, the tool is assumed capable of stroking the termination further. This modelling approach is more stable and more predictable than are the force controlled approach. In addition, setting the time scale really make sense since it is known beforehand how long time the stroking procedure will take. Finally, various load cases and parameter settings can be modelled with the same time scale ensuring that they will be easily comparable.

4.7 Mesh Convergence

The mesh has to be fine enough for the solution to converge with respect to element size. To investigate the mesh convergence status, simulations on a representative

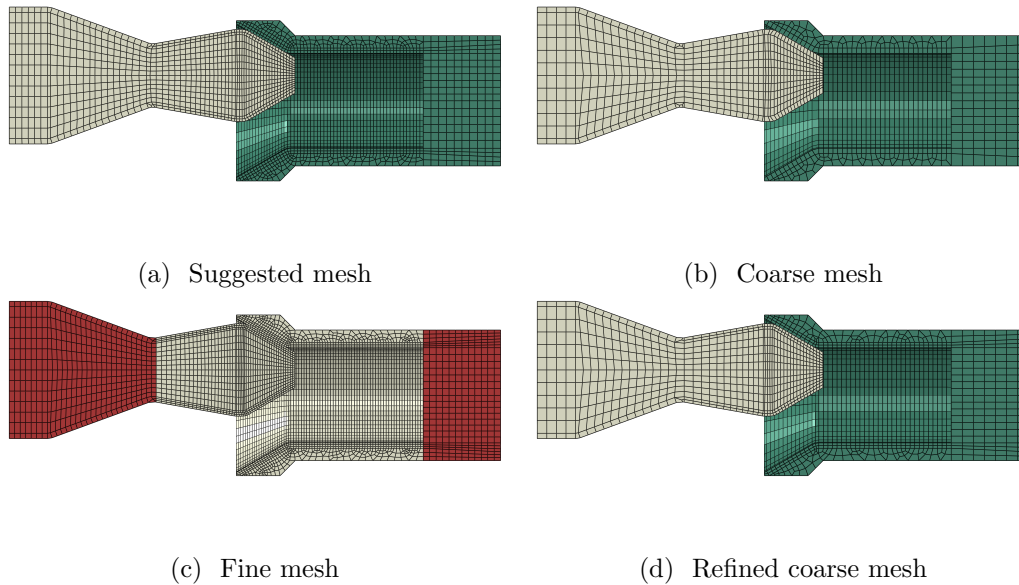


Figure 4.11: The different meshes that were tried out in the mesh convergence study. (a), (b) and (d) coloured by parts, (c) coloured by element type.

subset of the model are conducted for four different meshes. The model subset consists of the alignment rod and the alignment funnel (see Figure 2.1) initially positioned as in Figure 4.11a. In the figure only half the model subset is shown in order to better illustrate the mesh and the interaction of the two parts. The choice of the model subset to use in the mesh convergence study is based on pre-simulations discussed in Section 4.6, *Pre-simulations* where it was concluded that the funnel to rod interaction is critical from a computation point of view.

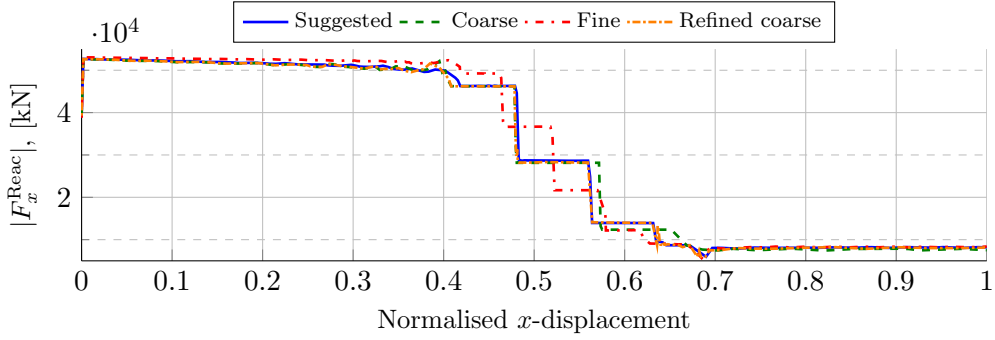
Figure 4.11b shows a coarse mesh with roughly 30% larger elements and Figure 4.11c shows a fine mesh with roughly 30% smaller elements. A coarse mesh with refinements in the critical contact area is shown in Figure 4.11d.

Figure 4.11c illustrates a mesh coloured by element type. Full integration elements are used in areas coloured white and reduced integration elements elsewhere. The settings for the four meshes are summarised in Table 4.4. The total number of elements for the model subset is varied from 9 952 to 50 770 and the corresponding number of nodes is altered from 12 118 to 56 571. The value shown in the column 'Seed' is the global element size setting expressed in millimetres. However, local seeds and the geometry of the parts imply that the numbers should only be taken as estimates of the actual element sizes. Further, the required CPU time, number of increments and number of iterations are included in the columns 'Time', 'Incrim' and 'Iter', respectively, to illustrate the performance of the different meshes. As can be seen the performance in terms of CPU time differs significantly.

The model subset includes an interaction between two non-flat surfaces, modelled with a surface-to-surface interaction. The normal behaviour is set to "hard contact" with a linear penalty, see Section 3.5, *Contact Interactions*. In the tan-

Table 4.4: Data for comparison of different mesh settings.

Mesh	Part	Elem #	Nodes #	Seed mm	Time s	Increm #	Iter #
Coarse	Funnel	4772	6056	16	1320	102	523
	Rod	5180	6062	13			
	Total	9952	12 118				
Refined Coarse	Funnel	7740	9260	16	4641	138	720
	Rod	6152	7049	13			
	Total	13 892	16 309				
Suggested	Funnel	15 810	18 414	12	9335	134	712
	Rod	13 020	14 584	10			
	Total	28 830	32 998				
Fine	Funnel	30 102	33 834	10	31 126	234	1196
	Rod	20 668	22 737	8			
	Total	50 770	56 571				

Figure 4.12: Magnitude of axial reaction force at rod end, F_x^{Reac} , for four different meshes.

genital direction a friction coefficient of $\mu = 0.12$ is set. Initially the end of the rod is clamped and the end of the funnel is constrained in all degrees of freedom except vertical translation. The rod-to-funnel contact supports the weight of half the termination and a quarter of the jumper, $1\,000\text{ kg} + 6\,250\text{ kg} = 7\,250\text{ kg}$. This is modelled as a force on the end of the funnel, pointing in negative z -direction. A load of is applied to the end of the funnel to represent the weight of the jumper and termination supported by the rod and funnel contact during assembling.

The stroking is modelled as an axial translation of the funnel in positive x -direction. Hence the funnel is forced upwards because of the interaction with the clamped rod. At the end of the rod, reaction forces in x - and z -direction as well as reaction moment in y -direction are extracted. The reaction force in the x -direction and reaction moment in y -direction are shown for all four meshes in Figure 4.12 and Figure 4.13, respectively. The forces and moments are plotted against normalised displacement of the end of the funnel in x -direction, x_{norm} .

In Figure 4.14 the initial position, two positions midway and the final position are shown. It is clear that for the last part of the simulation, $x_{\text{norm}} \in [0.7, 1]$, the

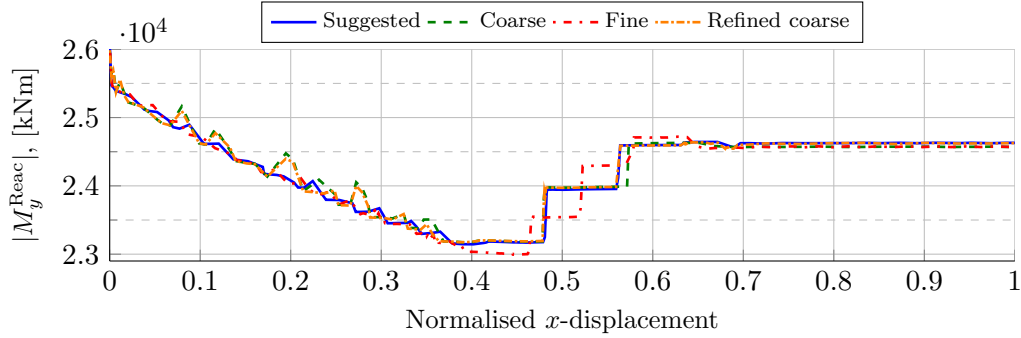


Figure 4.13: Magnitude of reaction moment at rod end, M_y^{Reac} , for four different meshes.

different meshes give very similar results, both for the reaction force, F_x^{Reac} , and the reaction moment, M_y^{Reac} . The contact is between two cylindrical surfaces and does not go through any changes during this phase, see Figure 4.14c and Figure 4.14d. For $x_{\text{norm}} \in [0, 0.4]$, the contact is between the conical surfaces of the rod and funnel, illustrated in Figure 4.14a. The reaction forces shown in Figure 4.12 indicates that all meshes performs approximately equally well while the reaction moments presented in Figure 4.13 speaks in favour for the suggested mesh and the fine mesh in this phase. The two coarser meshes show a couple of deviations from what should be a smooth curve. The stepwise behaviour that can be seen in both figures for $x_{\text{norm}} \in [0.4, 0.7]$ takes place between the two stages shown in Figure 4.14b and Figure 4.14c and appears when the contact “jumps” from one element to another. Hence the stepwise behaviour can only be removed through implementation of elements that are very small in x -direction. If elements are only resized in one direction, the quality of the elements may be reduced. Thus refining a mesh must be done to some extent in all three direction why a mesh that is refined enough to resolve the steps would imply a very large calculation cost.

The von Mises stresses in the contact area of the rod and funnel for $x_{\text{norm}} \approx 0.6$ are shown in Figures 4.15a to 4.15d. The main focus for this thesis is not to resolve the stresses but rather to investigate the behaviour of the system. However, in Section 4.6.3, *Material Implementation* it was concluded that using a material model with an elastic–plastic stress–strain relation resulted in a more stable solution with less noise. For this material model to be valid the stresses must be resolved “accurate enough” to make sense. As can be seen, the stress distribution for the suggested mesh shown in Figure 4.15a is similar to the stress distribution for the fine mesh depicted in Figure 4.15c. Also, the relative difference between the maximum value for the suggested mesh (660 MPa) and the corresponding value for the fine mesh (696 MPa) is only 5%. From the stress distribution for the coarse mesh, shown in Figure 4.15b, and the coarse mesh with refinements, Figure 4.15d, it can be concluded that the elements in these meshes are too large to resolve the stresses accurate enough. The relative errors for the maximum stress compared to the fine mesh are approximately 30% and 20%, respectively.

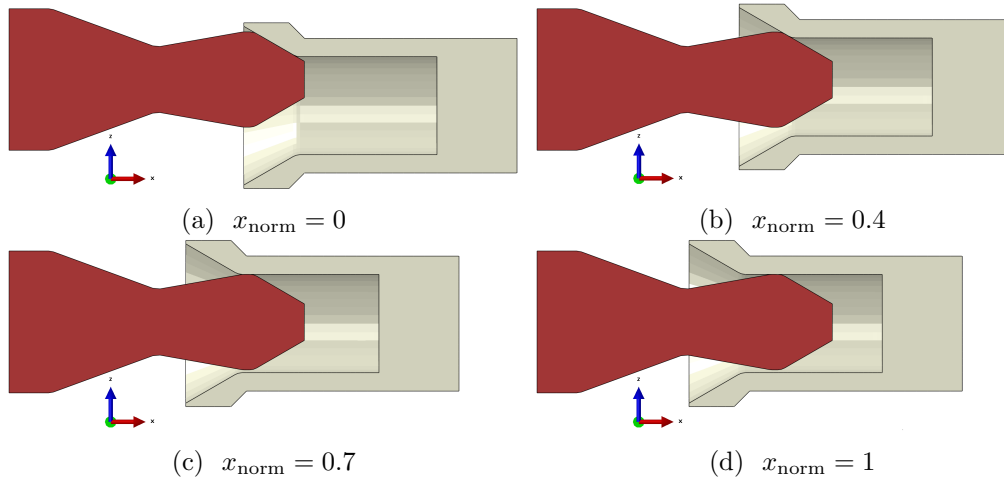


Figure 4.14: Four position along the path for the mesh convergence simulation.

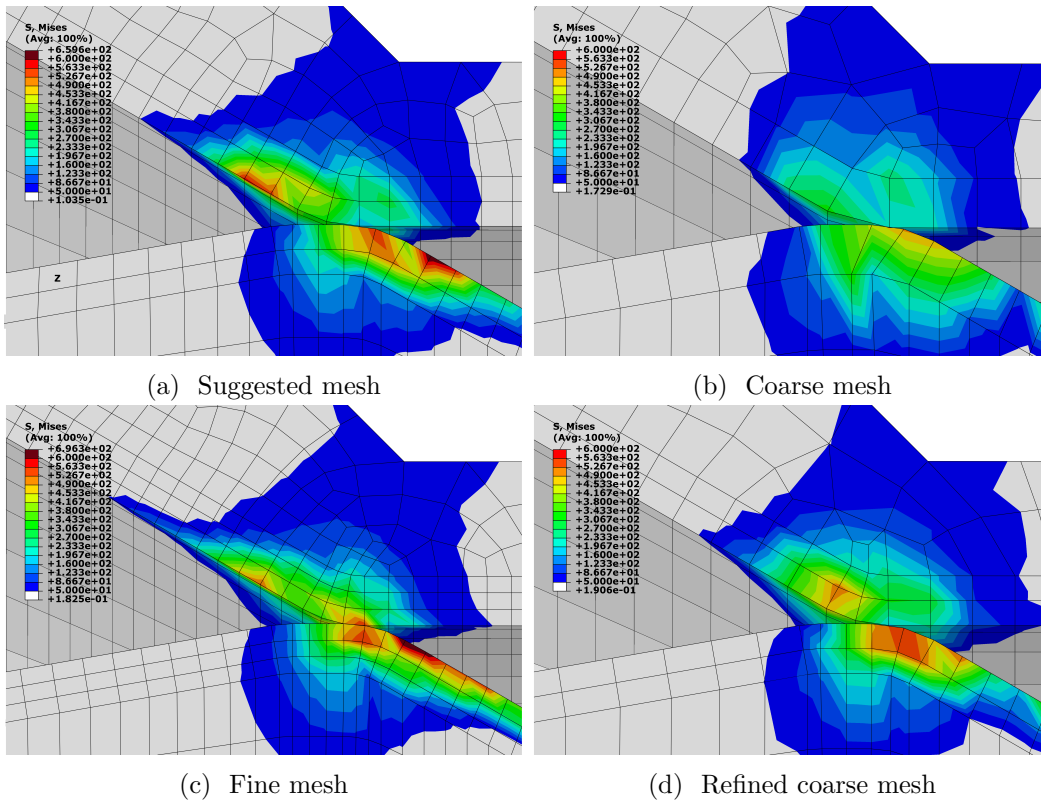


Figure 4.15: von Mises stresses at the critical contact area for the four different meshes, values given in MPa.

4.7.1 Concluding Remarks for Mesh Convergence

It can be concluded that the force balance is achieved for larger elements than is required to resolve the stresses. Since the analysis is not meant to be used for dimensioning but rather to find the critical load cases, a perfectly resolved stress field is not necessary. However, the stresses must be resolved accurate enough for the elastic–plastic material model to be valid. Consequently both the coarse mesh and the refined coarse mesh are considered too inaccurate. The suggested mesh performs well enough for the result to be regarded as valid and it is not worth the extra computation cost to fully implement a fine mesh.

Section 5

Results

The result presentation is divided into two parts. The first, presented in Section 5.1, *System Behaviour*, contains results that describe the load distribution and the system's behaviour. It begins with a description of how to interpret the results, whereafter the simulation results for various load cases are presented. All simulations for this part are conducted on the connector elements model.

In the second part, Section 5.2, *Model Evaluation*, the result for the comparison of the three models are presented. Also, an investigation of the computation cost is included.

5.1 System Behaviour

A simulation of the base load case applied to the connector elements model is used to interpret the load curves and the relation between them. Thenceforth, the response and sensitivity of the model is investigated through altering parameters and applying various load cases to the model. In Section 5.1.2, *Altering Jumper Stiffness*, the value of the parameter representing the jumper stiffness, κ_y , is altered. This analysis is used to evaluate the capacity of the system.

An illustration of the simulated stroking procedure is presented in Figure 5.20 at the end of this section. The figure illustrates the porch and termination at nine positions along the stroking path. The reader is encouraged to refer to this figure in order to better understand the results presented below.

5.1.1 Results Interpretation

In Figure 5.1 axial relative positions are shown for; the outboard hub with respect to the inboard hub, the outboard reaction plate with respect to the inboard reaction plate and the funnel with respect to the rod. As can be seen in the figure, the four curves describe almost the same change of position. This behaviour appears because the base case has no initial tilt and does not undergo any significant rigid body rotation during the stroking. However, the curves diverge slightly for s_h in the approximate interval [120, 180] mm. In this interval the funnel “climbs up” the rod and the termination is tilted slightly forward. The climb can be seen in Figure 5.2, where the vertical relative position for the outboard hub with respect to the inboard hub and for the funnel with respect to the rod are shown.

The tilt of the termination during the stroking procedure, measured at the center of the outboard hub, is plotted in Figure 5.3. The termination is leaned forward

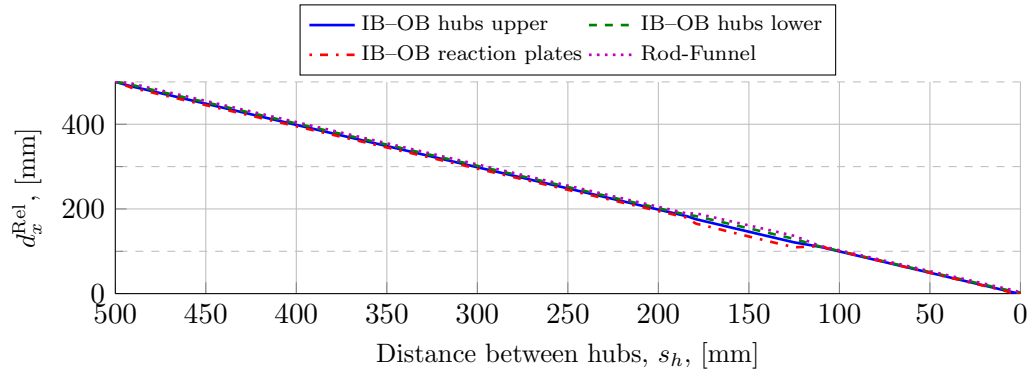


Figure 5.1: Relative positions in x -direction, d_x^{Rel} , for the base load case.

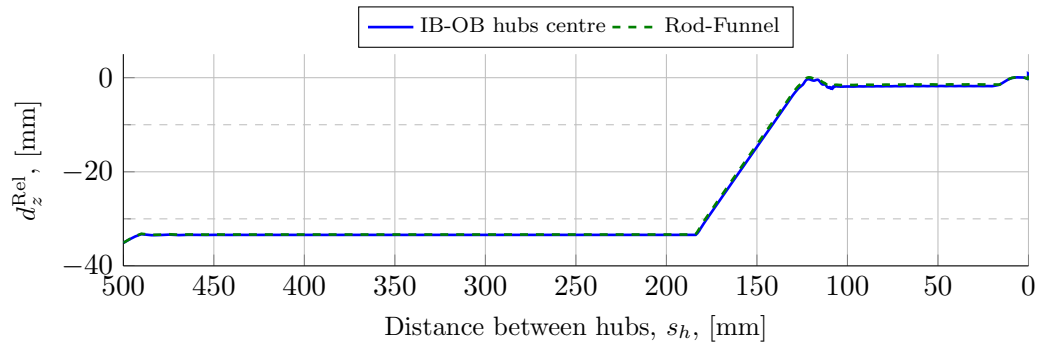


Figure 5.2: Relative positions in z -direction, d_z^{Rel} , for the base load case.

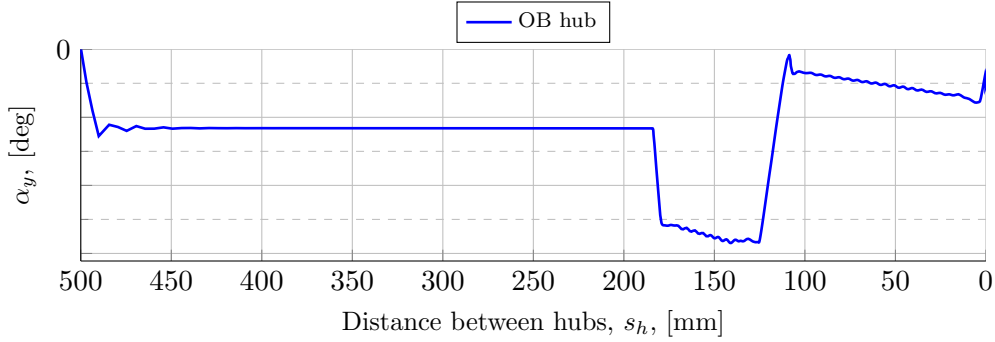


Figure 5.3: Tilt of the termination in y -direction, α_y , for the base load case. A negative value means tilt forward.

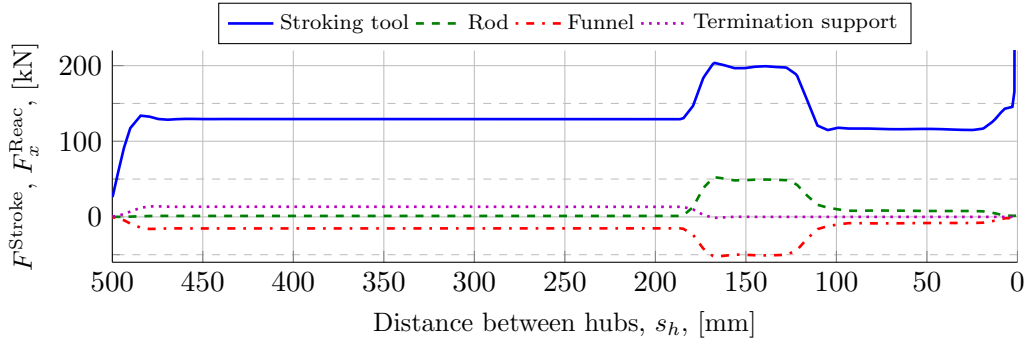


Figure 5.4: Required stroking force, F^{Stroke} and reaction forces in (local) x -directions, F_x^{Reac} , for the base load case.

when the funnel climbs the rod and abruptly reduced to almost zero thereafter.

In Figures 5.4 and 5.5 the reaction forces in (local) x -directions, F_x^{Reac} , and z -directions, F_z^{Reac} , respectively, are depicted for the rod, funnel and termination support¹. Also the required stroking force, F^{Stroke} , is shown in the Figure 5.4.

The axial reaction force in the funnel is first balanced by a reaction force in the funnel support. Thereafter, at $s_h \approx 180 s_h$, the contact between the rod and funnel is initialised and the reaction force in the funnel is instead balanced by a reaction force in the rod. This balance is kept to the very end of the stroking where the contact between the hubs are introduced, scarcely visible in the figure. The magnitude of the stroking force, F^{Stroke} , equals the magnitude of the reaction force in the funnel plus the magnitude of the back-tension, F^{BT} .

The same reasoning applies to the vertical reaction forces, depicted in Figure 5.5. The vertical reaction force denoted ‘Jumper’ is the vertical shear force with which the jumper affects the termination at the point where they connect. The major part of this force is simply the gravitational force due to the mass of the jumper, 12 500 kg, which equals a force of magnitude 123 kN.

¹Reaction forces and moments are defined in the coordinate systems local to the connector element used for the measure. See Section 4.5, *Definitions*

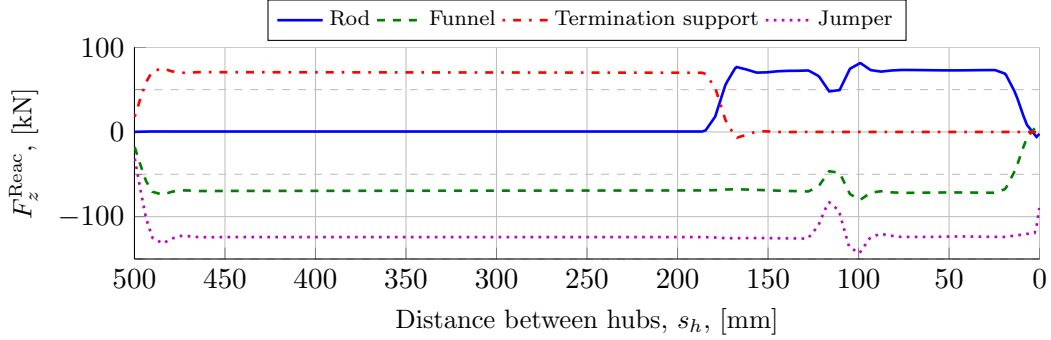


Figure 5.5: Reaction forces in (local) z -directions, F_z^{Reac} , for the base case.

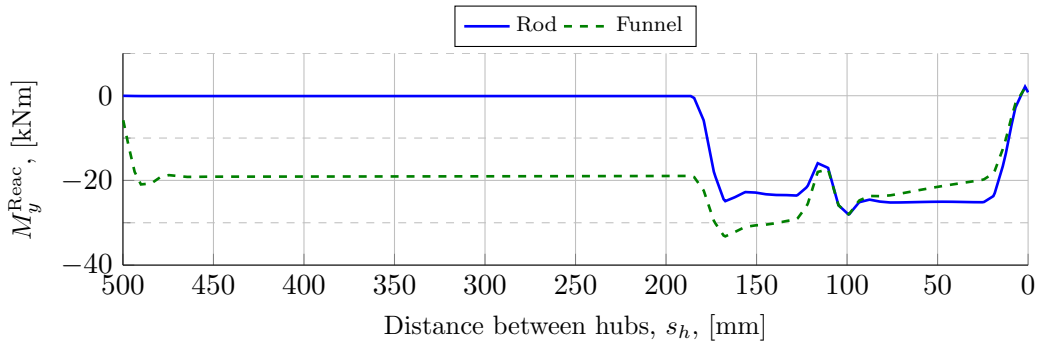


Figure 5.6: Reaction moments in (local) y -directions, M_y^{Reac} , for the base load case.

The reaction moments in the rod and funnel are shown in Figure 5.6 and the jumper moment is shown in Figure 5.7. For $s_h \in [20, 180]$ mm the reaction moment in the funnel and rod are approximately the same. The curve describing the funnel's reaction moment however has a slight slope while the curve for the rod is constant. This is due to the point of contact between the funnel and the rod is always located in the same position with respect to the rod; at the point where the rod's diameter is the largest. The contact point moves with respect to the funnel such that the leverage is decreased. Thus the reaction moment decreases too. At the very end of the stroking procedure, contact between the hubs is introduced why the reaction moments in the rod and funnel attachments vanish.

During the phase when the funnel climbs the rod, the stroking force is increased causing the termination to tilt forward additionally which in turn increases the jumper moment. When the funnel-to-rod contact passes the largest section of the rod, the required stroking force is abruptly decreased, and so are the axial reaction forces in the rod and funnel. This implies that the contributions from these forces to the moment equilibrium are reduced correspondingly. Hence the termination attains a more upright positions and the reaction force in the jumper is decreased. In Figure 5.3 this is seen as an abrupt decrease in tilt angle.

For $s_h \in [20, 100]$ mm the vertical reaction force at the funnel-to-rod contact con-

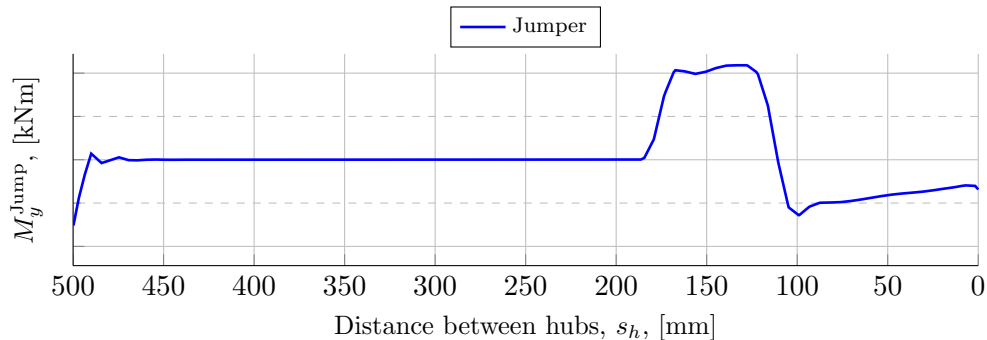


Figure 5.7: Jumper moment, M_y^{Jump} , for the base load case.

tributes to the moment equilibrium. As discussed above, the contact point moves with respect to the funnel and the leverage is decreased. The axial forces however, are constant during this phase. In order to maintain the moment equilibrium, the magnitude of the forward tilt increases which in turn implies that the reaction moment on the termination from the jumper is increased. This is seen in Figure 5.6.

If the jumper moment is too large, the required stroking force exceeds the capacity of the stroking tool before the stroking is finished. Consequently, the termination will not reach its final position and the hubs will not connect properly. However, supposing the hubs come within connector clamp catch² the stroke can be considered accepted. Since the stroking is modelled with a controlled displacement, the stroking tool capacity is in theory unlimited. To study whether or not the hubs are within catch when the stroking tool's capacity is reached, the relative positions of the hubs are plotted in Figure 5.8 on top of the stroking force for the last 50 mm of stroke. It can be seen in the figure that at the point at which the stroking tool capacity is exceeded, the measures between the hubs are small enough for the acceptance criterion presented in Section 2.2, *Stroking Acceptance Criterion* to be satisfied. Also the magnitude of the the outboard hub tilt, α_y , is sufficiently small. Note that the data for the reaction force in the stroking tool representation is unfiltered for this graph.

5.1.2 Altering Jumper Stiffness

Simulations on the connector elements model with the termination initially tilted $\alpha_y = \alpha_{y,s}^\circ$ (backward) and $\alpha_y = -\alpha_{y,s}^\circ$ (forward), respectively, are conducted for various degrees of jumper stiffness. This is obtained by altering the stiffness of the torsion spring attached to the end of the jumper representation, κ_y , between κ_1 kNm/deg and κ_8 kNm/deg.

The part of the jumper included in the analysis bends slightly why a $\alpha_{y,s}$ deg rotation of the termination does not imply a full $\alpha_{y,s}$ deg rotation of the end of the jumper representation to which the stiffness (torsion spring) is applied. Measured jumper moments, M_y^{Jump} , for the various load cases are shown in Figure 5.9 and

²See Section 2.2, *Stroking Acceptance Criterion* for a definition.

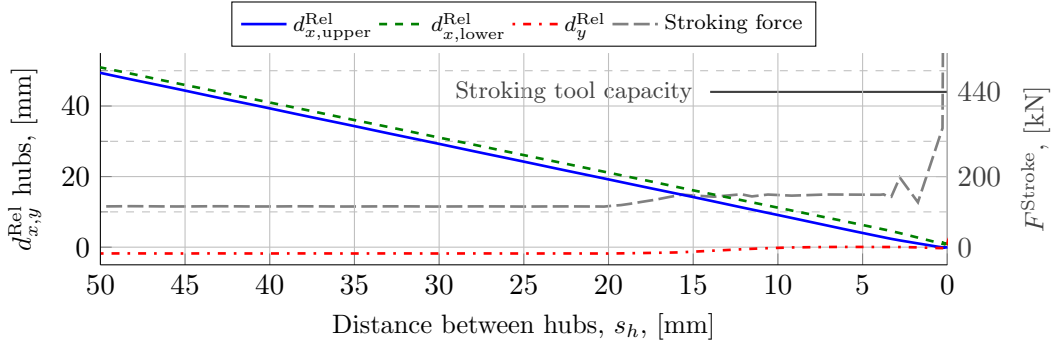


Figure 5.8: The hub's relative positions in x -direction (upper and lower hub face) and y -direction for the final 50 mm of stroking, for the base load case.

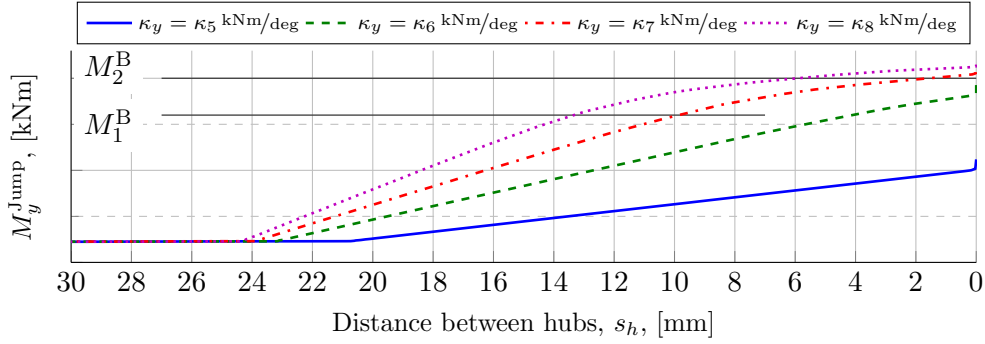


Figure 5.9: Jumper moment, M_y^{Jump} , for different degrees of jumper stiffness and $\alpha_y = \alpha_{y,s}^\circ$ initially (tilt backward). M_1^B and M_2^B indicate interpolated jumper moments calculated from the evaluation of the acceptance criterion, see Section 5.1.3, *Evaluation of Acceptance Criterion*.

Figure 5.10.

The tilt of the termination is depicted in Figure 5.11 for $\alpha_y = \alpha_{y,s}^\circ$ initial tilt (backward) and in Figure 5.12 for $\alpha_y = -\alpha_{y,s}^\circ$ initial tilt (forward). It can be seen that the termination guiding ensures that the path of the termination is almost the same for the last 20 mm and 50 mm of stroke, respectively for $\alpha_y = \alpha_{y,s}^\circ$ and $\alpha_y = -\alpha_{y,s}^\circ$, regardless of the jumper stiffness. The behaviour of the termination is the same for all degrees of stiffness, although the weaker the torsion spring the larger the tilt angle. This behaviour is common for several measures, both relative positions and reaction loads. Further, a smaller value of the stiffness yields significantly more noise.

In Figure 5.13 are the required stroking force, F^{Stroke} , during the last 30 mm of stroke for various degrees of jumper stiffness and $\alpha_y = \alpha_{y,s}^\circ$ initial tilt shown. Also, the relative position of the hubs, measured at the top and bottom of the hub faces are included in the figure. Due to the guiding of the termination, the relative positions, d_x^{Rel} , of the hubs are approximately the same for all values of κ_y . Hence the same

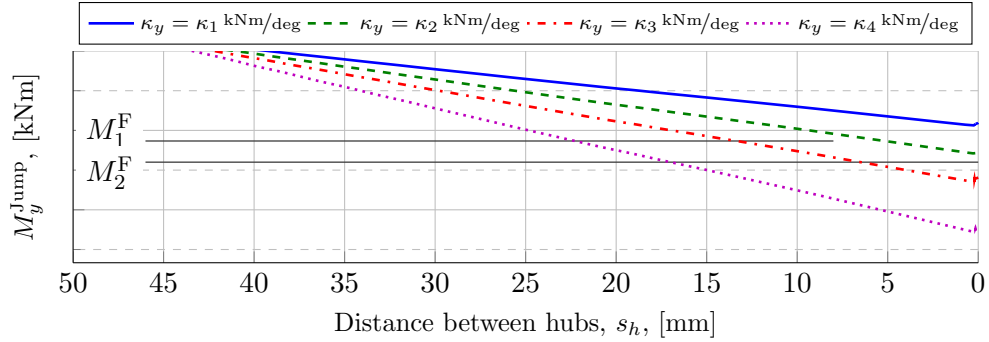


Figure 5.10: Jumper moment, M_y^{Jump} , for different degrees of jumper stiffness and $\alpha_y = -\alpha_{y,s}^\circ$ initially (tilt forward). M_1^F and M_2^F indicate interpolated jumper moments calculated from the evaluation of the acceptance criterion, see Section 5.1.3, *Evaluation of Acceptance Criterion*.

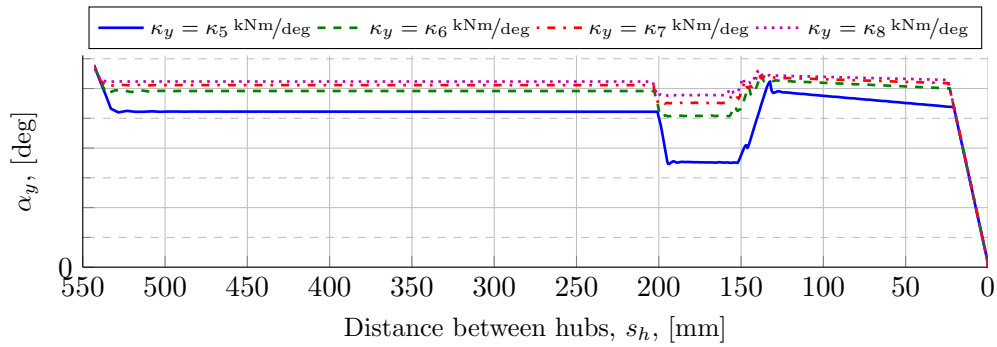


Figure 5.11: Tilt angle, α_y , for different degrees of jumper stiffness and $\alpha_y = \alpha_{y,s}^\circ$ initially.

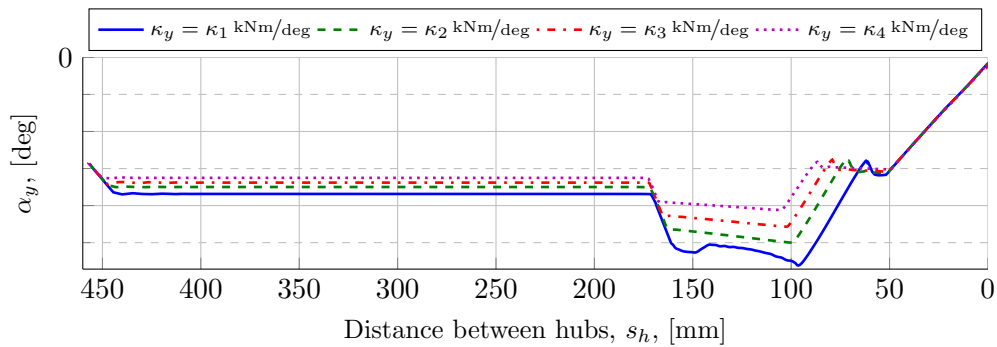


Figure 5.12: Tilt angle, α_y , for different degrees of jumper stiffness and $\alpha_y = -\alpha_{y,s}^\circ$ initially.

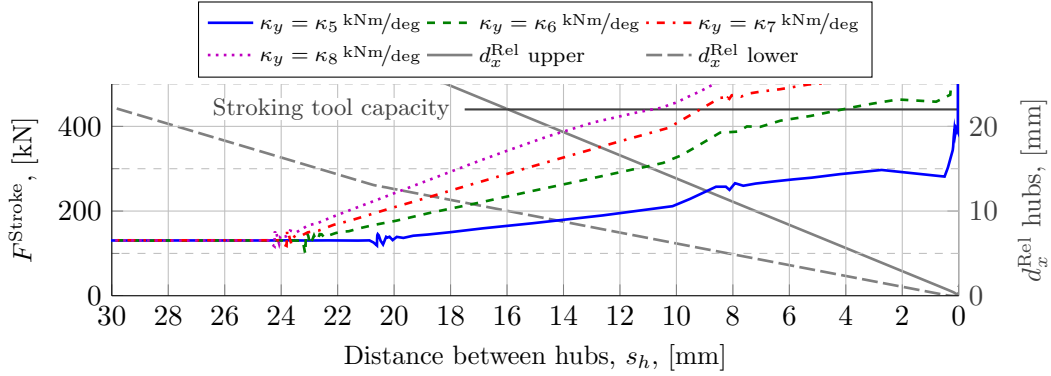


Figure 5.13: Required stroking force, F^{Stroke} , for different degrees of jumper stiffness and $\alpha_y = \alpha_{y,s}^\circ$ initially.

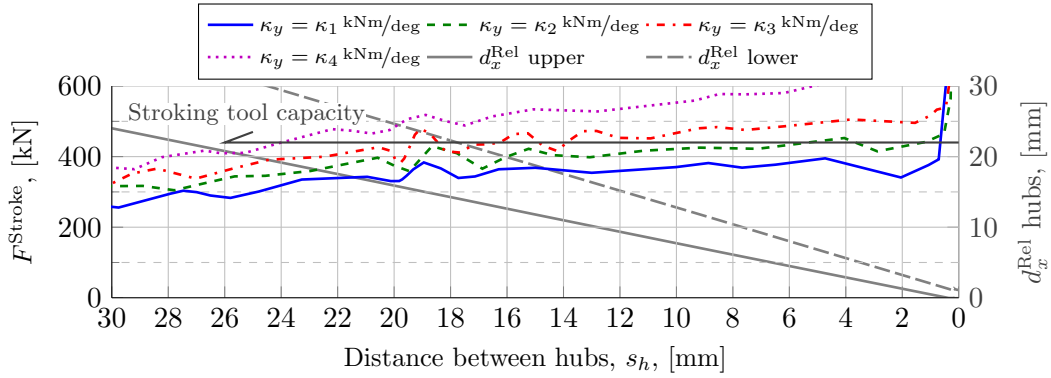


Figure 5.14: Required stroking force, F^{Stroke} , for different degrees of jumper stiffness and $\alpha_y = -\alpha_{y,s}^\circ$ initially.

d_x^{Rel} -curves can be used to evaluate the acceptance criterion for all load cases. Note that the curves for the stroking force are only mildly filtered in this figure to better capture the behaviour at the very end of the stroking. The corresponding figure for the load case with initial tilt forward is depicted in Figure 5.14.

5.1.3 Evaluation of Acceptance Criterion

According to the acceptance criterion the hubs are assumed to be within catch³ if the maximum distance between the hub faces is less than 10 mm and the misalignment angle is less than $\beta_{\text{catch}}^\circ$. From the data presented in Figure 5.11, it can be concluded that the tilt angle, α_y , falls below $\beta_{\text{catch}}^\circ$ for $s_h \leq 8$ mm for the back tilt case. For the front tilt case, α_y goes above $-\beta_{\text{catch}}^\circ$ for $s_h \leq 12$ mm, as can be seen in Figure 5.12.

For initial tilt backward, the upper relative position between the hub faces is the most critical. The 10 mm criterion is satisfied for $s_h = 7$ mm, which also implies that the criterion for α_y is fulfilled. The F^{Stroke} -curves in Figure 5.13 show that a

³Recall that the values given in this thesis are fictive values, used for illustrative purpose only.

jumper stiffness of $\kappa_y = \kappa_{67} \text{ kNm/deg}$ implies the stroking tool capacity is exceeded at $s_h = 7 \text{ mm}$. From Figure 5.9 it can be read that this corresponds to $M_y^{\text{Jump}} = M_1^{\text{B}} \text{ kNm}$ at $s_h = 7 \text{ mm}$ and $M_y^{\text{Jump}} = M_2^{\text{B}} \text{ kNm}$ at $s_h = 0 \text{ mm}$ ⁴.

Similarly for the front tilt load case, the relative hub positions plotted in Figure 5.14 indicates that the 10 mm hubs distance acceptance criterion is satisfied for $s_h = 8 \text{ mm}$, which in addition satisfies the criterion on α_y . Combining the F^{Stroke} -curves in Figure 5.13 and the M_y^{Jump} -curves in Figure 5.10 gives $M_y^{\text{Jump}} = -M_1^{\text{F}} \text{ kNm}$ at $s_h = 8 \text{ mm}$ and $M_y^{\text{Jump}} = -M_2^{\text{F}} \text{ kNm}$ at $s_h = 0 \text{ mm}$ ⁵.

To summarise; taking the reaction moment in the jumper at $s_h = 7 \text{ mm}$ and $s_h = 8 \text{ mm}$ for the backward tilt load case and the forward tilt load case, respectively, the calculated capacity of the system is

$$-M_1^{\text{F}} \text{ kNm} \leq M_y^{\text{Jump}} \leq M_1^{\text{B}} \text{ kNm}$$

where M_y^{Jump} is the allowed bending moment in y -direction applied to the termination at the end of the stroke. The calculation is based on $\alpha_y = \pm\alpha_{y,s}^\circ$ and a constant back-tension of 100 kN.

5.1.4 Altering Friction Coefficients

Three different friction coefficient settings were tried out through variations on the base load case on the connector elements model. The friction coefficients were decreased and increased, respectively, with 25 % which give the three settings: $(\mu_1, \mu_2) = (0.12, 0.20)$ (the settings for the base load case), $(\mu_1, \mu_2) = (0.09, 0.15)$ and $(\mu_1, \mu_2) = (0.15, 0.25)$. The required stroking force for the three settings are shown in Figure 5.15. It is clear that a 25 % increase of the friction coefficients does not imply a 25 % increase of the stroking force. This is because the reaction forces due to friction is only a small part of the resistance that counteracts the stroking force; the major part is the back-tension. The shape of the curves differs slightly at $s_h \approx 100 \text{ mm}$. At this point, axial reaction force due to the contact between the rod and funnel is decreased, the termination moves quickly and oscillations and noise appear. The variations seen in the figure is due to filtering of the oscillations and noise.

In Figure 5.16 the jumper moment, M_y^{Jump} , is depicted. The curves have similar shape but different magnitude. This is due to the termination tilt in y -direction varies slightly for the different settings.

The magnitude of F^{Stroke} and M_y^{Jump} at three positions along the stroke path, $s_h = 50 \text{ mm}$, $s_h = 150 \text{ mm}$ and $s_h = 400 \text{ mm}$, are shown in Figures 5.17a and 5.17b. Each of these positions lies within a section of the stroking path in which the relation between F^{Stroke} or M_y^{Jump} and the friction coefficients is approximately linear. Approximations of the slopes relations, $\partial F^{\text{Stroke}}/\partial\mu$ and $\partial M_y^{\text{Jump}}/\partial\mu$, in each section are given in Table 5.1. Note that only one friction coefficient at the time is

⁴The values are obtained by linear interpolation between simulation data for $\kappa_y = \kappa_6 \text{ kNm/deg}$ and $\kappa_y = \kappa_7 \text{ kNm/deg}$ at $s_h = 7 \text{ mm}$ and $s_h = 0 \text{ mm}$, respectively.

⁵The values are obtained by linear interpolation between simulation data for $\kappa_y = \kappa_2 \text{ kNm/deg}$ and $\kappa_y = \kappa_3 \text{ kNm/deg}$ at $s_h = 8 \text{ mm}$ and $s_h = 0 \text{ mm}$, respectively.

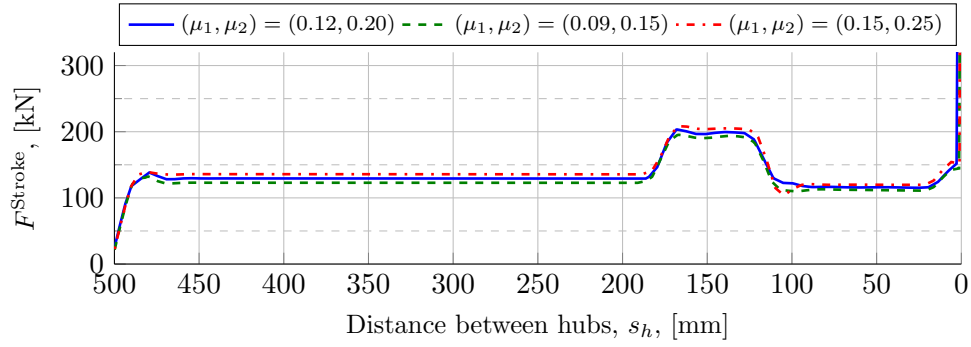


Figure 5.15: Required stroking force, F^{Stroke} , for three different settings on the friction coefficients, μ_1 and μ_2 .

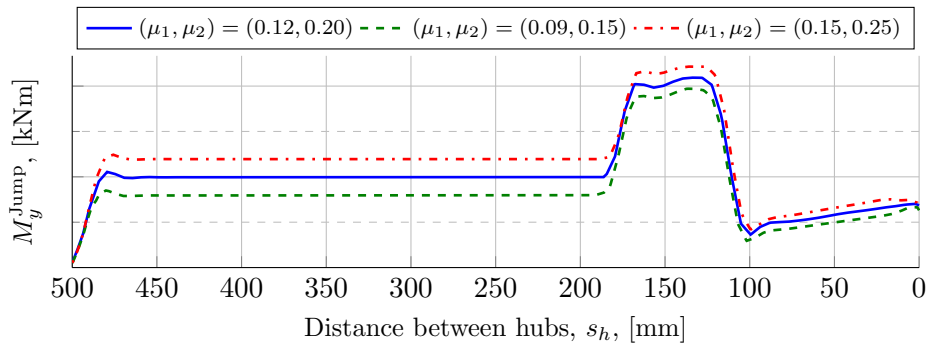


Figure 5.16: Jumper moment, M_y^{Jump} , for three different settings on the friction coefficients, μ_1 and μ_2 .

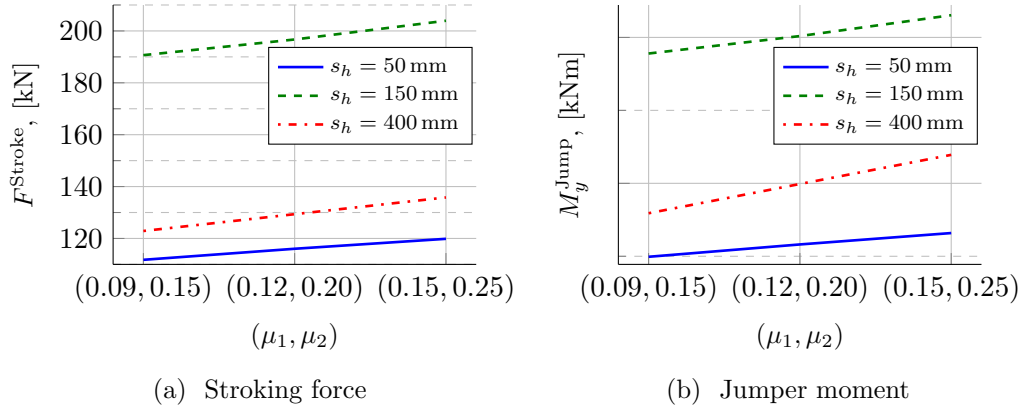


Figure 5.17: The sensitivity of the connector elements model with respect to friction coefficients at three s_h -values.

Table 5.1: The sensitivity of F^{Stroke} and M_y^{Reac} with respect to friction coefficients.

$s_h \in$	$\partial F^{\text{Stroke}} / \partial \mu_1$	$\partial F^{\text{Stroke}} / \partial \mu_2$	$\partial M_y^{\text{Jump}} / \partial \mu_1$	$\partial M_y^{\text{Jump}} / \partial \mu_2$
[20, 90]		133 kN/1		$\partial M_{y,1}^{\text{Jump}}$ kNm/1
[125, 170]	225 kN/1		$\partial M_{y,2}^{\text{Jump}}$ kNm/1	
[190, 450]	130 kN/1		$\partial M_{y,3}^{\text{Jump}}$ kNm/1	

“active” and affects the solution. The values describe the sensitivity of F^{Stroke} and M_y^{Jump} with respect to the friction coefficients.

5.1.5 Back-tension Modelling

As described in Section 4.1.6, *Base Load Case*, the back-tension, F^{BT} , is implemented to allow it to be modelled as a constant force or a displacement dependent spring force (see equation (4.1)). Below is a comparison of the base load case (modelled with a constant force) and two load cases with spring forces of different stiffness. All three load cases are modelled on a connector elements model. Recall that the constant force in the base load case is 100 kN. The degrees of stiffness for the displacement dependent back-tensions are 0.2 kN/mm and 0.3 kN/mm, corresponding to the forces 100 kN and 150 kN, respectively, at 500 mm displacement.

Because the stroking is modelled as a controlled displacement, the differences between the load cases in axial displacements (x -direction) and vertical displacement (y -direction), are very small. Instead the stroking forces required to obtain the specified displacements vary according to Figure 5.18. It is clear that the choice of modelling technique is not critical during the stroke since the required stroking force is significantly lower than the stroking tool capacity (not shown in figure) except for the very last millimetres. The capacity is exceeded for $s_h \leq 2$ mm (obtained from unfiltered data) for all three models, which imply that the hubs are within connector clamp catch. It can further be seen that the difference between the base

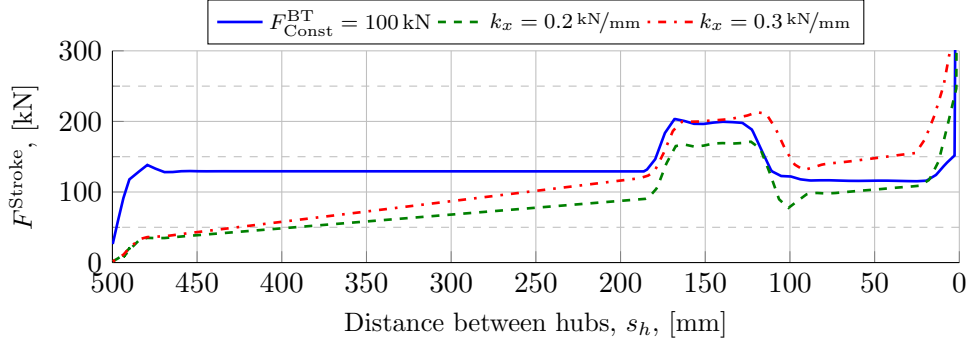


Figure 5.18: Required stroking force, F^{Stroke} , for the base load case with jumper back-tension as constant force, $F^{\text{BT}} = F_{\text{Const}}^{\text{BT}}$, compared to two load cases with jumper back-tension modelled with spring forces, $F^{\text{BT}} = k_x \cdot (500 - s_h)$.

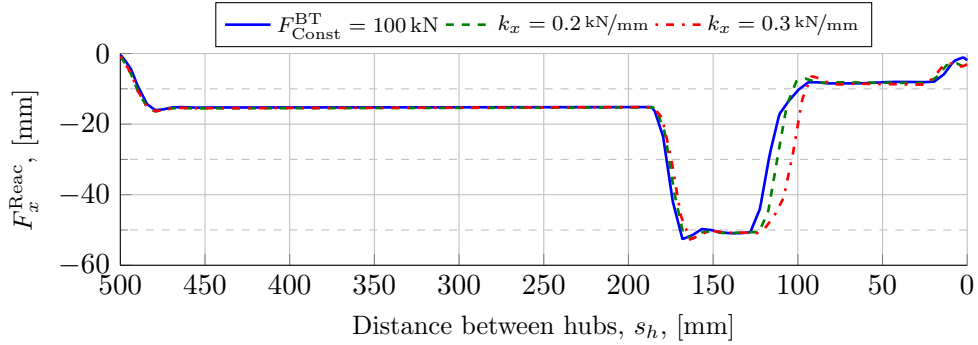


Figure 5.19: Axial reaction force in funnel, F_x^{Reac} , for the base load case with jumper back-tension as constant force, $F^{\text{BT}} = F_{\text{Const}}^{\text{BT}}$, compared to two load cases with jumper back-tension modelled with spring forces, $F^{\text{BT}} = k_x \cdot (500 - s_h)$.

load case curve and any of the spring force curves can be closely approximated by the relationship

$$F_{\text{Base}}^{\text{Stroke}}(s_h) - F_{\text{Spring}}^{\text{Stroke}}(s_h) \approx k_x \cdot (s_h - 500) + 100 \quad \text{kN} \quad (5.1)$$

where k_x is the current jumper stiffness.

Further, the reaction forces on the individual parts can be studied. The axial reaction force on the funnel is taken as example here and is depicted in Figure 5.19. Other reaction loads, both axial and vertical forces and moments for the rod, termination support and hubs behave similar. It can be seen in the figure that the differences between the reaction forces are very small.

It is worth to stress that modelling the back-tension as a displacement dependent force, here $F^{\text{BT}} = k_x \cdot (500 - s_h)$, implies that $F^{\text{BT}} = 0$ initially, for $s_h = 500$. Consequently, the balancing moment, described in Section 4.1.4, *Loads*, has to be recalculated. During the stroking, the back-tension is increased and the moment

equilibrium is disrupted. To maintain moment equilibrium the forward tilt is (in this case) increased as compared with the constant back-tension load case. Since the funnel is located approximately 500 mm below outboard hub centre, where s_h is measured, a larger forward tilt implies that the rod-to-funnel contact takes place for smaller s_h -values. This is visible in Figure 5.19 at $s_h \approx 170$ mm and, in particular, at $s_h \approx 120$ mm.

The balancing moment remains a part of the reaction moment in the jumper representation throughout the entire stroking. For load cases with zero initial tilt, the balancing moment and the reaction moment in the jumper at the very end of the stroke are in theory equal. Due to numerical errors and deformations in the structure this is not quite true. But still, the simulations show that the theoretical equivalence is approximately satisfied.

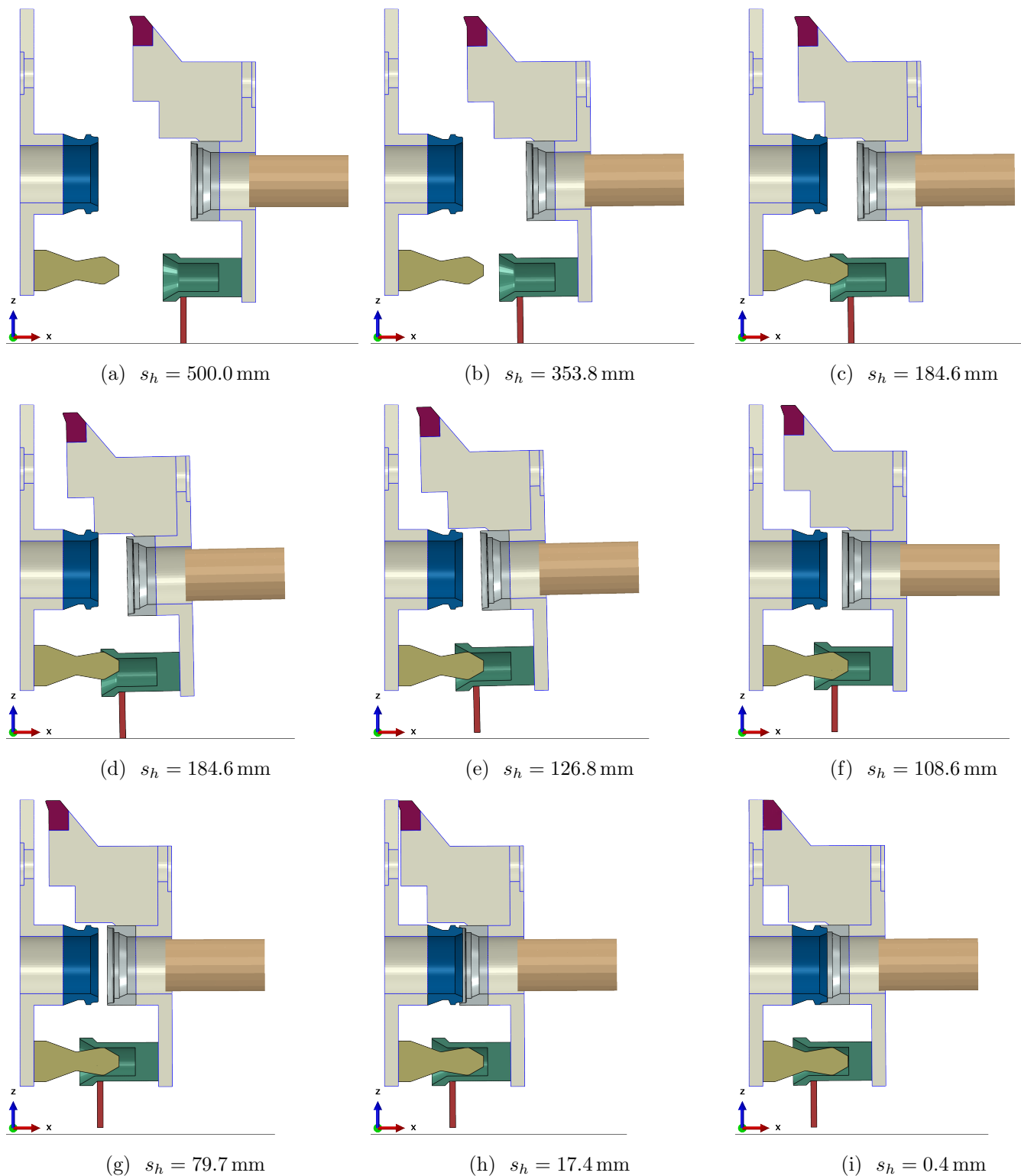


Figure 5.20: The simulated stroking procedure for the base load case on the symmetric connector elements model. In the figure, display representations of the reaction plates (white parts) are included to make the illustration clearer.

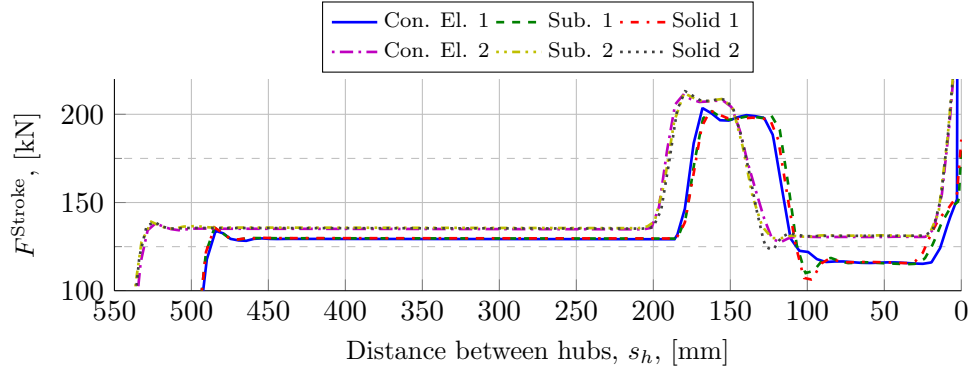


Figure 5.21: The required stroking force, F^{Stroke} , for two different load cases (1 and 2) and three different models with reaction plates modelled with; connector elements, substructures and solid parts. Note the scale on the y -axis.

5.2 Model Evaluation

Results from all three models are analysed in order to investigate the implications when modelling the reaction plates with; rigid connector elements, substructures or solid parts. Various load cases are chosen as basis for the study, whereof the results from two are used to evaluate the result accuracy of the models; the base load case (1) and $\alpha_y = \alpha_{y,s}^\circ$ initial tilt (backward) with all other settings as the base load case (2). For the analysis of the computation cost, also a load case with $\alpha_y = \alpha_{y,s}^\circ$ initial tilt (backward) and double the value of the torsion spring representing the jumper stiffness, $\kappa_y = 2 \cdot \kappa^{\text{Base}} \text{ kNm/deg}$.

5.2.1 Results Comparison

In Figure 5.21 the required stroking forces for the three models and two load cases are plotted. The different length of the stroking is due to different starting positions for the base load case and the load case with initial tilt. The jumper moment is plotted for the various models and load cases in Figure 5.22.

It can be seen that the curves have practically the same magnitudes. However, it is worth to point out that the data shown here are filtered. The unfiltered data shows significantly more noise for the connector elements model due to the stiffer reaction plates.

Reaction loads measured at other locations behave similar and no significant differences between the models are observed. Also, the relative positions in x -direction show only small deviations, less than a few percent. The vertical relative positions of the hubs however, clearly indicates that the connector elements model is stiffer and does not sag in the same way as the other two models when positioned on the landing frame. The curves for the substructures model and the solid parts model indicates they are similar, with the substructures model being marginally stiffer. At $s_h = 50 \text{ mm}$, the results for the connector elements model differs almost 10 % from

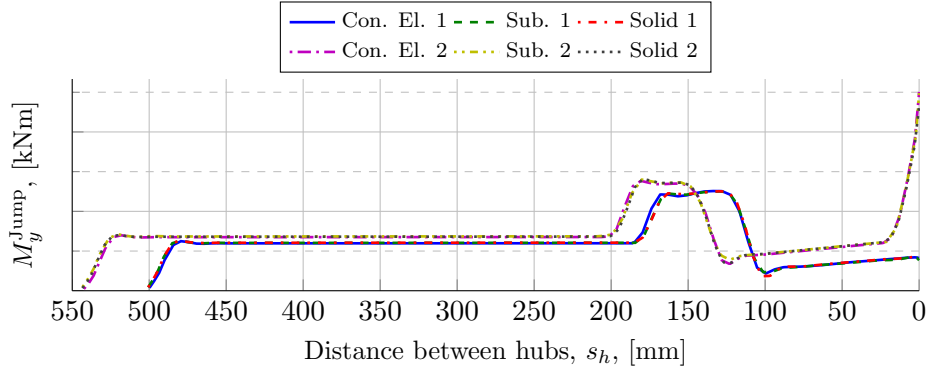


Figure 5.22: Jumper moment as felt by the termination, M_y^{Jump} , for two different load cases (1 and 2) and three different models with reaction plates modelled width; connector elements, substructures and solid parts.

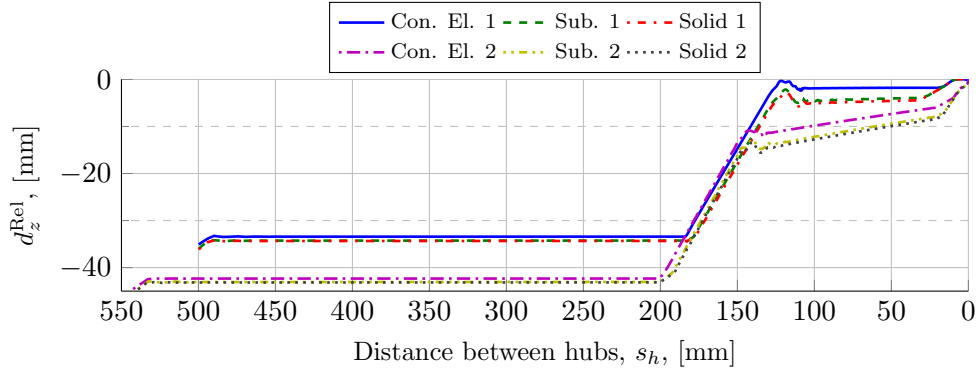


Figure 5.23: Relative positions of the hubs, d_z^{Rel} , for two different load cases (1 and 2) and three different models with reaction plates modelled width; connector elements, substructures and solid parts.

the result for the solid parts model. The substructure model differs less than 2%. In Figure 5.23, the relative positions of the hubs in z -direction are shown.

5.2.2 Computation Cost

The base load case and the $\alpha_{y,s}^\circ$ initial tilt load case, and in addition a load case with $\alpha_{y,s}^\circ$ initial tilt and double the value of κ_y , simulated with the connector elements model, the substructures model and the solid parts model are used to investigate the computation cost for the various models. In Table 5.2 the computation times are summarised. All simulations are run on 16 CPUs on the same computer.

It can be seen that both the substructures model and the solid parts model requires less number of increment and less number of iterations than the connector elements model⁶. On average for the three load cases, the substructures model

⁶The number of iterations is the total number, that is the sum of the discontinuity iterations and the equilibrium iterations for the entire simulation.

Table 5.2: Computation cost comparison for the three models.

<i>Model</i>	<i>Increments</i>	<i>Iterations</i>	<i>CPU time [s]</i>	<i>Wall clock time [h]</i>	<i>CPU time per incr. [s]</i>	<i>CPU time per iter. [s]</i>
Base load case						
Con. El.	444	2247	42 043	1.47	94.7	18.7
Sub.	426	2308	38 884	5.42	91.3	16.8
Solid	378	1975	57 182	1.96	151.3	29.0
$\alpha_y = \alpha_{y,s}^\circ$ initial tilt (backward)						
Con. El.	619	3055	57 130	2.00	92.3	18.7
Sub.	533	2738	45 775	6.56	85.9	16.7
Solid	486	2436	68 172	2.34	140.3	28.0
$\alpha_y = \alpha_{y,s}^\circ$ initial tilt, increased jumper stiffness						
Con. El.	625	3147	59 556	2.07	95.3	18.9
Sub.	564	2933	49 025	7.07	86.9	16.7
Solid	505	2530	73 236	2.54	145.0	28.9

requires 91 % of the iterations and 95 % of the increments required by the connector elements model. The corresponding numbers for the solid parts model are 81 % and 83 %, respectively.

It can further be seen that the solid parts model requires the most CPU time for all load cases, followed by the connector elements model and last the substructure model. However, the required wall clock time shows a different picture; the substructure model requires significantly longer computation time than the other two models. On average, the solid parts model requires 124 % of the wall clock time required by connector elements model. The corresponding number for the substructures model is 346 %.

The CPU time per increment and CPU time per iteration vary similarly since the number of iterations per increment is approximately constant for all models and all load cases. The CPU time per iteration is independent of the specific load case (except for numerical effects) and thereby indicates the computation cost of the equation system related with the model. A further discussion on this topic can be found in Section 6.2.2, *Computation Cost*.

Section 6

Discussion

The discussion below is divided into two sections, corresponding to Section 5.1, *System Behaviour* and Section 5.2, *Model Evaluation*, in which the results are discussed further. Also, suggestion for improvements of the models and the simulations are discussed.

6.1 System Behaviour

This first section discusses the behaviour of the connector element model and the interpretation of the results. Thenceforth the sensitivity with respect to some uncertain parameters, a complication due to the inclusion of the jumper part and the acceptance criterion are discussed.

6.1.1 Interpretation

The load curves presented in Section 5.1.1, *Results Interpretation* give valuable information about how the system behaves. Although only the last part of the stroking is limiting the capacity, the reaction loads throughout the entire stroking procedure give useful information for evaluating the designs of the individual parts. As an example, redesigning the rod such that the transition from inclined to horizontal profile at the point where the rod has its largest diameter becomes more smooth is likely to regularise the movement of the termination. In turn, the abrupt decreases in tilt angle, α_y , as seen in Figure 5.3, as well as in jumper moment, M_y^{Jump} , visible in Figure 5.6, will likely be reduced. This is desirable, not only from a simulation point of view. The smoother the stroking procedure is, the less the risk that the termination gets stuck or jams.

The loads on the rod and funnel can be used for dimensioning and design improvement of these parts as well as the reaction plates. However, it must be taken into consideration that the simulations presented in this thesis are performed on a symmetry model. A full model subject to angular misalignment around the vertical axis (z -axis) will cause the rod-to-funnel contact on one side to be initialised prior to the other. If the jumper is stiff, the termination will begin to climb the first rod before contact is initialised between the second rod and funnel and the entire termination will rest on one single rod-to-funnel set.

In general, the system's capacity is determined by the very last part of the stroking. For load cases with initial tilt, the termination is pulled to its upright position at the very end of the stroke which generates a moment in the jumper.

However, both the model and the simulation settings are a bit too coarse to capture small details at this stage. A suggestion to improve the accuracy, at least to some extent, without rebuilding the model is to replace the last part of the stroking step with an additional step implemented with smaller step size. It may also be possible to implement the additional step as force driven, which would simplify the evaluation of the acceptance criterion. An optional solution is to simulate the last part of the stroke in a separate more detailed analysis, possibly with a refined model, taking the positions and loads at a point close the end in this analysis as initial condition.

6.1.2 Sensitivity

In Sections 5.1.2, *Altering Jumper Stiffness*, 5.1.4, *Altering Friction Coefficients* and 5.1.5, *Back-tension Modelling* the sensitivity of the model with respect to uncertain parameters is investigated. The parameters used for the base load case are not calibrated with physical tests. Altering the friction coefficients, which are now implemented with “standard” values, has a linear impact on the axial reaction forces and on the reaction moments. Further, it affects the entire stroking path.

Altering the value of the torsion spring representing the bending stiffness of the jumper, on the other hand, does not have a large impact on reaction loads or relative position (except for the tilt angle) along the stroking path. If the termination is initially tilted it does, however, significantly affect the required stroking force at the very end of the stroking since the termination has to be pulled to its upright position.

Modelling the back-tension in different ways indicates that only the stroking force, F^{Stroke} , jumper moment, M_y^{Jump} , and tilt angle, α_y , are significantly affected in terms of magnitude. The reaction loads in rod, funnel and hubs are slightly delayed for the displacement dependent back-tensions due to difference in tilt angle. From Figure 5.18 and Figure 5.19 it can be concluded the jumper back-tension and stroking force are approximately cancelled out and the remaining loads (except for the reaction moment in the jumper) are not significantly affected. This conclusion is valid as long as the stroking is modelled with a controlled displacement.

6.1.3 Jumper Modelling

It was suggested by AKS to include a part of the jumper spool in the simulation. The purpose was to stabilise the model, reduce noise and give a more realistic result. Unfortunately, the inclusion of the jumper had some complicating implications. It is desirable to have a straightforward relation between the tilt angle, α_y , and the magnitude of the jumper moment, M_y^{Jump} , since it simplifies the evaluation of the acceptance criterion. This is of particular interest when results are interpolated or extrapolated. A linear relation implies that the validity of extrapolated results are significantly increased.

It can be assumed that the moment on the termination equals the sum of the applied balancing moment M^{Bal} and the moment due to tilt, $M_y^{\text{Tilt}} = -\alpha_y \cdot \kappa_y$. However, including the part of the jumper spool complicates the relation. Since the jumper spool representation bends slightly, the relation between the jumper moment

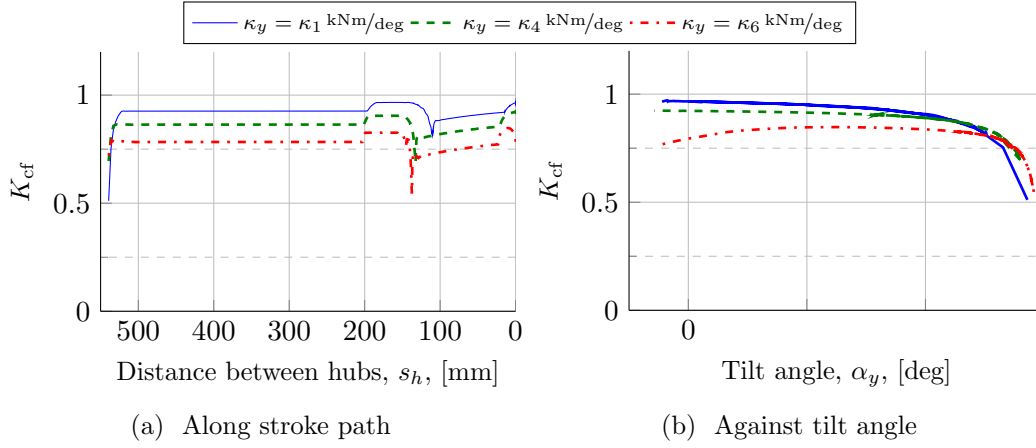


Figure 6.1: Correction factor, K_{cf} , against s_h and α_y for three different degrees of stiffness for the torsion spring representing jumper stiffness, κ_y and initial tilt $\alpha_y = \alpha_{y,s}^\circ$.

and the tilt angle becomes

$$M_y^{\text{Jump}} = M^{\text{Bal}} - \alpha_y \cdot \kappa_y \cdot K_{cf}(\alpha_y, \kappa_y, \dots) \quad (6.1)$$

where K_{cf} is a correction factor. Displacements in the termination may affect the value of K_{cf} as well, but to a significantly less degree than α_y and κ_y .

K_{cf} can be solved from equation (6.1) and calculated from the simulation data. Calculated values for K_{cf} for a load case with $\alpha_{y,s}^\circ$ initial tilt backward are shown in Figure 6.1. The value of K_{cf} depends on the difference between the rotation angle that affects the torsion spring, attached to the very end of the jumper spool representation, and the tilt angle, measured at the outboard hub's centre.

A suggestion for future analyses is to avoid the part representing the jumper spool and attach the torsion spring directly to the termination reaction plate in order to get better control of the relation between initial tilt angle and the jumper moment at the end of the stroke.

6.1.4 Evaluation of Capacity

In Section 5.1.3, *Evaluation of Acceptance Criterion*, it is described how the capacity of the system can be calculated from the obtained simulation data. It is worth to stress that the acceptance criterion is based on purely geometrical conditions. The clamp connector does have capacity limitations too, which has not been considered in this thesis.

From the stroking force curves for the backward tilt load case in Figure 5.13 it is clear that increasing the capacity of the stroking tool increases the capacity of the entire system. Increasing the capacity by 14 %, from 440 kN to 500 kN, increases the capacity of the system (the allowed jumper moment) from M_1^B kNm to M_3^B kNm, or by almost 18 %. Softening the acceptance criterion, on the other hand, does not affect the capacity to the same extent. Assuming the criterion for the hub face

distance is increased from 10 mm to 15 mm, or by 50 %, the capacity of the system is increased by less than 13 %, from M_1^B kNm to M_4^B kNm (given that the criterion for maximum allowed misalignment angle is increased correspondingly).

Also the capacity for the load case with initial tilt forward, as seen in Figure 5.14, is increased if the stroking tool's capacity is increased. Increasing the stroking tool's capacity with 14 % increases the capacity of the system from $-M_1^F$ kNm to $-M_3^F$ kNm, or with 27 %. Softening the criterion for the hub face distance by 50 % only increases the capacity with 1.2 %, to $-M_4^F$ kNm.

This behaviour, both for backward initial tilt and forward initial tilt, is due to small geometrical changes in the model. Although the acceptance criterion is modified with a 50 % change, contributions to the moment equilibrium from the stroking force and the back-tension are approximately the same. Hence the maximum allowed jumper moment becomes approximately the same too. The small increases in capacity are due to minor differences in friction forces at the hub face contact and at the rod-to-funnel contact. Note that increasing the capacity of the stroking tool may cause other problems, such as strength problems with the tool itself, the reaction plates or the hub lips. The discussion is included here in order to estimate the sensitivity of the system's capacity with respect the stroking tool's capacity and the acceptance criterion.

Compared with results from a previous test of a similar systems [2], the results obtained in this analysis are reasonable. The capacity obtained in [2] is

$$-M_{\text{lower}}^{\text{Test}} \text{ kNm} \leq M_y^{\text{Jump}} \leq M_{\text{upper}}^{\text{Test}} \text{ kNm},$$

where M_y^{Jump} is the allowed bending moment that acts on the termination. Taking the jumper moment at point where the stroking tool's capacity is exceeded as reference, the calculated capacity in this analysis is

$$-M_1^F \text{ kNm} \leq M_y^{\text{Jump}} \leq M_1^B \text{ kNm}$$

where $M_1^B \approx 0.8M_{\text{upper}}^{\text{Test}}$ and $M_1^F \approx 1.7 \cdot M_{\text{lower}}^{\text{Test}}$, (calculated for 3° initial tilt forward and backward, respectively, and a constant back-tension of 100 kN). A possible explanation to why the difference between the lower limits is larger is that the values of κ_y has to be significantly lower for the forward tilt load case than for the backward tilt load case. Hence the model becomes less stiff and more sensitive to small inaccuracies, for example due to the discretisation.

Note that this acceptance criterion is based on the assumption of an initial tilt angle of $\alpha_y = \pm\alpha_{y,s}^\circ$. A different setting might give a slightly different result. The weaker the jumper stiffness is, the larger the initial tilt angle has to be to correspond to the same jumper moment after the termination is rotated to its upright position. Furthermore, a small initial tilt angle and a large stiffness implies that the stroking force and the jumper moment increase more rapidly at the very end of the stroke than if the opposite is true.

The jumper moment obtained at $s_h = 0$ mm does not represent the capacity of the system with respect to the stroking tool but rather the capacity of the entire system. However, for this capacity to be valid, it must be evaluated against the capacity of the clamp connector.

6.2 Model Evaluation

Below are the comparison of the three models discussed in terms of accuracy and computation cost.

6.2.1 Results Comparison

In Section 5.2.1, *Results Comparison* three models and two load cases are compared. The vertical relative positions shown in Figure 5.23 clearly indicate that the connector elements model is stiffer than the other two models. The sag in the substructures half model and the solid parts half model is mostly due to weaker attachments of the rod and funnel, which implicate they undertake small rigid body rotations in addition to the deformation. Deformations of the reaction plates in vertical direction are very small.

The small differences between the models indicates that replacing the reaction plates with connector elements or substructures are valid simplifications, given that the solid parts model is correct. However, it must be stressed that also the solid parts model is a simplification of the structure, with several parts eliminated. The possibility to verify the models, either with results from physical tests or with a more detailed simulation, would therefore be valuable.

The graphs presented in Section 5.2.1, *Results Comparison* show filtered data, for which the differences between the models are small. Unfiltered data on the other hand, shows that the connector element model is subject to significantly more noise, in particular for measures of loads on the rod and funnel when contact is initialised and deinitialised. By definition, a filter delays the input signal and, in general, the delay varies over the frequency domain [4]. Hence it is desirable to filter the signals as little as possible, both due to delay and in order not to lose information. Otherwise the increase of the stroking force might be delayed too much and the acceptance criterion is incorrectly satisfied.

Furthermore, it is worth to point out that one benefit that substructures imply has not been utilised here. As mentioned in Section 3.6, *Substructures*, a substructure gives the opportunity to redesign the part without changing its interface to the surrounding environment. In this analysis, the purpose of using substructures is mainly to reduce the computation cost. Possible benefits with interchangeable parts have therefore not been considered.

6.2.2 Computation Cost

In Section 5.2.2, *Computation Cost* it is concluded that the substructures half model has the lowest computation cost with respect to CPU time, but requires approximately three times as much wall clock time as the other two models. The reason is that Abaqus[®] cannot parallelise the calculations of a simulation containing substructures in the same way as if no substructures are present. In each iteration, Abaqus[®] performs several tasks. One of them is the element operations in which the strains and stresses within each element are calculated for a given displacement, element type and material model. Another is the solver; the displacement vector is

calculated given the applied forces and the mass, damping and stiffness matrices. If substructures are present only the solver can be executed through thread-based parallelisation in Abaqus[®]. Thus, for a particular number of CPUs, the computation cost does not gain much from increasing the number further.

The connector elements model requires the most increments for all three load cases. This is a clear indication that the connector elements model is stiffer and produces more noise than the other two. The substructures model and the solid parts model require little more than five iterations per increment for all load cases. The number for the connector elements model is a little lower. Probably due to the smaller increments.

It can further be seen that required CPU time per increment and CPU time per iteration are approximately constant for each model, regardless of which load case is simulated. The solid parts half model requires the most CPU time per iteration since it has the most elements. Noteworthy is that the substructures half model requires less CPU time than the connector elements half model for all three load cases, both per increment and per iteration, although the number of elements and variables are the same (approximately). The enlarged computation cost for the connector elements half model indicates that the equation system for this model is, in some sense, harder to solve. Possible explanations are that the connector elements are implemented in a different way, using Lagrangian multipliers. Furthermore, the solver uses numerical methods designed especially for sparse matrix problem. Although the two models have the same number of element and variables, the matrices can have different bandwidth and thereby do not require the same number of computations.

To summarise, there are four aspects that affect the overall performance of a model. First, the CPU time per iterations indicates how computationally hard the equation system related with the model is to solve. CPU time per iteration is independent of the load case except for numerical aspects¹. Second, the number of iterations per increment determines how long time it will take to calculate one increment. This number is rather constant since Abaqus[®] updates the increment step size after each increment. Third, the required number of increments depends on the stability of the model and the amount of noise produced by it. Also, it might vary for different load cases. Fourth and finally, the capacity of the computer and the possibility to parallelise the calculation.

¹For example, the number of non-zero elements in the matrices affects the required amount of data to be stored and the efficiency of the solver.

Section 7

Concluding Remarks

The obtained load curves increase the understanding of how the system behaves and are valuable for illustrative purposes. To accurately evaluate the capacity of the system, a more detailed simulation of the last part of the stroking path is eligible. Initial conditions for such an analysis can be extracted from the results of this analysis. Furthermore, the load curves give useful inputs when evaluating the design of individual parts.

Removing the jumper part and attach the torsion spring to the termination would simplify evaluation of the acceptance criterion since a more straightforward relation between the jumper moment, M_y^{jump} , and the tilt angle, α_y , can be established. This would reduce the number of required interpolations and thereby increase the accuracy of the evaluation.

The shape of the stroking force curves used for evaluating the acceptance criterion indicates that increasing the stroking tool capacity with 14% increases the capacity of the system with 18% and 27%, respectively, for forward tilt and backward tilt load cases. However, this may imply other problems such as strength problems with the reaction plates and the stroking tool itself. A redesign of the hubs and clamp connector in order to increase the maximum allowed clearance for catch by 50% would increase the capacity of the system for backward tilt load cases with approximately 13% but does only increase the capacity for forward tilt load cases with a little more than 1%.

Modelling the reaction plates with connector elements or substructures are valid simplifications. As compared with the solid parts model, the results for the substructures model differs only a few percent while for the connector elements model, the results varies up to about 10% for some measures. On the one hand, by carefully consider which measures that are of interest, the connector elements model may give a sufficiently good result. On the other hand, the reduction in computation cost for the connector elements model is too small to justify that it should be used over the solid parts model in general; only about 20%.

The substructures model is the most cost effective model with respect to CPU time. It requires about two third of the CPU time required by the solid parts model. However, it requires almost three times as much wall-clock time due to limitations in Abaqus[®]. If it is possible to execute the simulation in parallel to a larger degree than was done in this analysis, for example on a cluster, the substructures model would be best choice since it would be by far the most cost effective and would give almost the same results as the more costly solid parts model.

Bibliography

- [1] Aker Solutions AB. Internal report.
- [2] Aker Solutions AB. Internal report.
- [3] Aker Solutions AB. Mouthly communication.
- [4] G. Bianchi. *Electronic Filter Simulation & Design*. McGraw-Hill Education, 2007.
- [5] R.D. Cook, D.S. Malkus, and M.E. Plesha. *Concepts and Applications of Finite Element Analysis*. John Wiley & Sons, 3 edition, 1989.
- [6] W Kuntjoro, AMH Abdul Jalil, and J Mahmud. Wing structure static analysis using superelement. *Procedia Engineering*, 41(0):1600 – 1606, 2012.
- [7] N.S. Ottosen and H. Petersson. *Introducation to the Finite Element Method*. New York: Prentice Hall, 1992.
- [8] Simulia, Dassault Systems. *Abaqus 6.13, Abaqus/CAE User's guide*, 2013.
- [9] Simulia, Dassault Systems. *Abaqus 6.13, Analysis User's guide, Volume 1: Introduction, Spatial Modeling, Execution & Output*, 2013.
- [10] Simulia, Dassault Systems. *Abaqus 6.13, Analysis User's guide, Volume 2: Analysis*, 2013.
- [11] Simulia, Dassault Systems. *Abaqus 6.13, Analysis User's guide, Volume 3: Materials*, 2013.
- [12] Simulia, Dassault Systems. *Abaqus 6.13, Analysis User's guide, Volume 4: Elements*, 2013.
- [13] Simulia, Dassault Systems. *Abaqus 6.13, Analysis User's guide, Volume 5: Prescribed Conditions, Constraints & Interactions*, 2013.
- [14] Simulia, Dassault Systems. *Abaqus 6.13, Theory Guide*, 2013.
- [15] E. Tzimas, A. Georgakaki, C. Garcia-Cortez, and S.D. Petevs. Enhanced oil recovery using carbon dioxide in the european energy system. Technical Report EUR 21895 EN, European Comission, Institute for Energy, 2005.